Chemical Engineering Journal 426 (2021) 130801

Contents lists available at ScienceDirect

Chemical Engineering Journal

journal homepage: www.elsevier.com/locate/cej

Enhanced photocatalytic activity of accordion-like layered Ti_3C_2 (MXene) coupled with Fe-modified decahedral anatase particles exposing {1 0 1} and {0 0 1} facets

Anna Grzegórska [a,*], Paweł Głuchowski [b], Jakub Karczewski [c], Jacek Ryl [c], Izabela Wysocka [a], Katarzyna Siuzdak [d], Grzegorz Trykowski [e], Katarzyna Grochowska [d], Anna Zielińska-Jurek [a,*]

[a] Department of Process Engineering and Chemical Technology, Faculty of Chemistry, Gdańsk University of Technology, G. Narutowicza 11/12, 80-233 Gdańsk, Poland
[b] Institute of Low Temperature and Structural Research, Polish Academy of Sciences, Okólna 2, 50-422 Wrocław, Poland
[c] Institute of Nanotechnology and Materials Engineering, Faculty of Applied Physics and Mathematics, Gdańsk University of Technology, G. Narutowicza 11/12, 80-233 Gdańsk, Poland
[d] Centre for Plasma and Laser Engineering, The Szewalski Institute of Fluid-Flow Machinery, Polish Academy of Science, Fiszera 14, 80-231 Gdańsk, Poland
[e] Faculty of Chemistry, Nicolaus Copernicus University, Gagarina 7, 87-100 Toruń, Poland

ARTICLE INFO

Keywords:
Carbamazepine
MXene
Decahedral anatase particles
Titanium carbide
{1 0 1} facet
{0 0 1} facet

ABSTRACT

New composites consisting of decahedral anatase particles exposing {0 0 1} and {1 0 1} facets coupled with accordion-like layered Ti_3C_2 with boosted photocatalytic activity towards phenol and carbamazepine degradation were investigated. The photocatalysts were characterized with X-ray diffraction (XRD), diffuse reflectance spectroscopy (DR/UV–Vis), Brunauer-Emmett-Teller (BET) specific surface area, Raman spectroscopy, scanning electron microscopy (SEM), electron paramagnetic resonance (EPR) spectroscopy, emission spectroscopy, luminescence decay analysis, electrochemical impedance spectroscopy (EIS), transmission electron microscopy (TEM), X-ray photoelectron spectroscopy (XPS), thermogravimetric analysis (TGA), and electrophoretic mobility measurements. The effect of hydrothermal reaction parameters on physicochemical, structural, and photocatalytic properties was studied. In all photodegradation processes, *ortho*-hydroxyphenol and *para*-hydroxyphenol were detected as the first intermediates of phenol decomposition. For the TiO_2/Ti_3C_2(140,12) sample containing V_{Ti}, a higher concentration of *para*-hydroxyphenol than *ortho*-hydroxyphenol was observed, whereas for sample TiO_2/Ti_3C_2(220,24) higher concentration of *ortho*-hydroxyphenol was noticed. The formation of surface heterojunction between {1 0 1} and {0 0 1} facets of decahedral anatase particles grown on Ti_3C_2 surface led to improved photoelectron transfer and enhanced photocatalytic activity towards degradation of carbamazepine - non-biodegradable and susceptible to bioaccumulation in living organisms commonly used pharmaceutical agent. Moreover, modification of TiO_2/Ti_3C_2 surface with iron by magnetron sputtering deposition markedly improved photocatalytic activity in carbamazepine decomposition, with nearly 100% degradation in 60 min of irradiation under simulated solar light.

1. Introduction

Pollution of the aqueous environment with organic compounds from year to year becomes a more significant problem globally. According to the European Environmental Agency report, only about 38% of surface waters are in good chemical condition [1]. There are various organic compounds with potentially adverse health effects on living organisms emitted to the environment, including nonsteroidal anti-inflammatory drugs, antibiotics, hormones, plasticizers, antimicrobials, or surfactants [2].

Among the group of emerging contaminants, carbamazepine (CBZ) is an efficient anticonvulsant and neuropathic painkiller [3] frequently detected in wastewaters in concentrations range from 1 to 3600 ng/dm^3, while in pharmaceutical effluents reaches even up to 443 mg/dm^3 [4]. The CBZ is a low biodegradable and high persistent compound. Thus only below 10% of its content is effectively removed at conventional wastewater treatment plants [5]. Moreover, some recent studies confirmed CBZ toxicity for sludge microbial activity and aquatic

* Corresponding authors.
E-mail addresses: anna.grzegorska@pg.edu.pl (A. Grzegórska), annjurek@pg.edu.pl (A. Zielińska-Jurek).

https://doi.org/10.1016/j.cej.2021.130801
Received 10 January 2021; Received in revised form 13 May 2021; Accepted 7 June 2021
Available online 11 June 2021

organisms like bacteria, algae, invertebrates, and fish [6]. Various methods have been proposed for carbamazepine degradation, including ozonation, extraction, membrane-based separation, or biological processes [7–11]. Furthermore, special attention has been paid to photocatalytic degradation of emerging contaminants and persistent organic pollutants as an efficient and green technology [12].

Heterogeneous photocatalysis is a sustainable and promising strategy intensively investigated for water splitting [13], bacterial disinfection [14], carbon dioxide reduction to energy fuels [15], and degradation of persistent organic pollutants for environment purification [16]. However, it is still challenging to design a durable photocatalyst highly active in solar light (UV–Vis).

The surface chemistry of a photocatalyst is one of the most crucial parameters influencing semiconductor material's surface properties and photocatalytic activity. The most commonly used method to inhibit electron-hole pairs recombination and enhance Vis light activity is a modification of semiconductors, primarily TiO_2 nanoparticles with noble metal nanoparticles [17]. Noble metal nanoparticles (NMNPs) may improve the photocatalytic activity in UV–Vis light due to surface plasmon resonance properties and prolong photo-induced charge carriers due to the formation of Schottky's barrier at the semiconductor–metal interface. Moreover, NMNPs facilitate electron transport by the equilibration of the Fermi levels [17]. Nonetheless, this method is relatively expensive, and the photocatalytic activity of semiconductor material strongly depends on noble metal nanoparticles morphology (size and shape), which is also determined by the reaction environment [18]. Thus less cost and more straightforward solutions are still in demand.

Recently, two-dimensional (2D) materials have attracted great interest in various fields, including electrocatalysis, energy storage, sensors, and photocatalysis [19–23]. Highly anisotropic 2D semiconductors characterized with atom-level thickness, tunable composition, and well-defined structure may offer many desirable properties such as enhanced electron-hole separation, high mobility of charge carriers, and also reduced charge carriers recombination rate [24–25]. The 2D materials possess an improved surface to volume ratio and, as a consequence, significantly developed surface area. Furthermore, 2D semiconductor materials with exposed {1 0 1} and {0 0 1} facets are expected to play a crucial role in enhancing the photocatalytic degradation of emerging contaminants. Another approach is creating interfacial heterojunction to induce an internal electric field, enhancing charge carriers separation [26–29].

MXene compounds with graphene-like morphology have become promising materials instead of platinum or palladium as a noble-metal-free co-catalyst. The MXene group consists of transition metal carbides, nitrides, or carbonitrides [30]. Wei et al. [31] reported the potential application of Ti_3AlC_2 as support for uniform nucleation of lithium particles for Li-based batteries. MXenes are materials with advantageous lithiophilicity, flexibility, mechanical robustness, and good electronic conductivity [31–32]. Due to its properties close to metallic, MXenes may create a Schottky barrier at the MXenes-semiconductor interface and enact as a reservoir for photo-generated electrons [33]. Moreover, they may improve photocatalyst stability, carrier density, and light absorption over a broader spectrum [34–35]. Hybrid MXene photocatalysts have been already successfully combined with Bi_2WO_6 [36], CdS [34], ZnS [37], Ag_3PO_4 [38], g-C_3N_4 [39], Cu_2O [40], BiOBr [41], Fe_2O_3 [42], and TiO_2 [43]. Furthermore, some MXene-derived materials such as MXene/AuNPs, MXene/PdNPs may be prepared by a cost-effective self-assembly technique. The self-assembled composites are characterized by tunable nanoparticles size with uniformly dispersed particles on the MXene substrate, well-controlled by optimized reaction time [44–48]. The application of MXene as a co-catalyst reported in the literature focused on the photocatalytic removal of dyes from the aqueous environment [49–50], hydrogen generation, and CO_2 reduction [51–53].

In this regard, in the present study, MXene compound – $Ti_3C_2T_x$ was used for in-situ preparation of composite photocatalyst consisting of decahedral anatase particles (DAPs) and titanium carbide (Ti_3C_2). DAPs with eight equivalent {1 0 1} facets and two {0 0 1} facets are expected to reveal improved photocatalytic activity. The exposed facets determine photocatalytic activity and degradation pathway of emerging organic pollutants. Therefore, the influence of surface structure properties of TiO_2/Ti_3C_2 layered composite on photocatalytic activity was studied in detail. Moreover, for the first time, in this study, new Fe-modified composites prepared through magnetron sputtering deposition on decahedral anatase particles exposing {0 0 1}, {1 0 1} facets coupled with Ti_3C_2 were obtained and applied for photocatalytic degradation of phenol - a model organic pollutant and carbamazepine anticonvulsant and neuropathic painkiller, which belongs to the group of emerging organic contaminants. The effect of synthesis temperature and time on TiO_2/Ti_3C_2 and Fe-modified TiO_2/Ti_3C_2 composites structural properties and photocatalytic activity was investigated.

2. Experimental

2.1. Materials

The MXenes matrix Ti_2AlC-Ti_3AlC_2 (50 μm) was purchased from NANOGRAFI Co. Ltd. Hydrofluoric acid (48%), and tetrafluoroboric acid (48 wt% in H_2O used for synthesis were purchased from Sigma Aldrich. Phenol (99%) and carbamazepine were purchased from Sigma Aldrich. Scavengers: benzoquinone (reagent grade, ≥ 98%) and *tert*-butanol (anhydrous, ≥ 99.5%) were purchased from Sigma Aldrich, POCH Gliwice provided $AgNO_3$ (pure p.a.) and EDTA (pure p.a.). Alfa Aestar provided nickel (II) oxide (99.998% metals basis) to determine sample crystallinity. Deionized water (DI) was used in all experiments. All reagents were used as received without further purification.

2.2. Preparation of $Ti_3C_2T_x$

$Ti_3C_2T_x$ (T_x – termination groups -O, –OH, and -F) matrix was prepared by selective etching of the Al layer from Ti_3AlC_2. In this regard, 1 g of Ti_2AlC-Ti_3AlC_2 powder was dispersed in 10 cm^3 of 48% HF solution and continuously stirred at room temperature for 24 h. In the next step, the obtained suspension was centrifuged and washed with DI water until the pH of 7 (neutral pH). The resulting powder was dried under air condition at 80 °C to dry mass.

2.3. Preparation of TiO_2 /Ti_3C_2 layered composite

In a typical experiment, TiO_2/Ti_3C_2 composites were prepared by dispersing 0.4 g of Ti_3C_2 in 59.2 cm^3 DI water and sonication for 10 min to agglomerates breakdown. Then, 0.8 cm^3 of HBF_4 was added dropwise under magnetic stirring. The dispersion was stirred for 30 min and transferred to a 200 cm^3 Teflon-lined stainless-steel autoclave reactor. The reaction temperature was selected from 140 °C to 220 °C. The reaction time equaled 6, 12, or 24 h. The final photocatalyst was centrifuged and washed with DI water until the pH of 7 (neutral pH). Then the sample was dried under air condition at 80 °C to dry mass.

2.4. Preparation of Fe- TiO_2/Ti_3C_2 composite

The Fe-TiO_2/Ti_3C_2 composites were prepared according to the procedure described in paragraph 2.2. The TiO_2/Ti_3C_2 sample was synthesized at 140 °C for 12 h and 220 °C for 24 h. In the next step, thin layers of TiO_2/Ti_3C_2 were applied on the glass slide and dried at 80 °C for 1 h. Iron deposition on the TiO_2/Ti_3C_2 surface was conducted using a magnetron sputtering system (Q150S, Quorum Technologies, Lewes, UK) with mounted highly pure Fe target (99.5%, EM-Tec). The Fe thickness was controlled by quartz microbalance and implemented the program and set to 20 nm.

2.5. Characterization of TiO_2/Ti_3C_2 and Fe- TiO_2/Ti_3C_2 photocatalysts

The crystallinity and average crystallite size were investigated by X-ray powder diffraction. The analysis was performed using Rigaku Intelligent X-ray diffraction system SmartLab (Rigaku Corporation, Tokyo, Japan), equipped with a sealed tube X-ray generator operating with Cu Kα radiation 40 kV and 30 mA. Scans were recorded in the 2θ range from 5° to 80°, with a speed $2°min^{-1}$ and a step of 0.01°. The crystalline and amorphous phase content was analyzed using an internal standard - NiO.

Nitrogen adsorption–desorption isotherms were measured at 77 K (boiling point of liquid nitrogen) with the Micromeritics Gemini V apparatus (model 2365) (Norcross, GA, USA). The surface area and pore volume were determined by the multipoint BET method. Before each measurement, the samples were degassed at 200 °C under a constant flow of nitrogen. The nitrogen isotherm was measured in a partial pressure range from 0.05 to 0.3.

Diffuse reflectance (DR/UV–Vis) spectra were recorded in the wavelength range from 200 nm to 800 nm using a ThermoScientific Evolution 220 spectrophotometer (Waltham, MA, USA). As a reference, barium sulfate was used. The photocatalysts bandgap energy was calculated from the corresponding Kubelka-Munk function, $(R)^{0.5}E_{ph}^{0,5}$ against E_{ph}, where E_{ph} is photon energy.

Electron paramagnetic resonance (EPR) spectroscopy was used to investigate the structural defects of TiO_2/Ti_3C_2 composites. The EPR analysis was performed at room temperature in a RADIOPAN SE/X-2547 spectrometer. EPR measurements were conducted at X-band (≈ 8.9 GHz), employing a reflection resonator with a modulation frequency of 100 kHz.

The composites' surface morphology was examined by scanning electron microscopy (SEM) using SEM Microscope FEI Quanta FEG 250. Moreover, the images and selected area electron diffraction (SAED) patterns were obtained for the most photocatalytic active samples using the transmission electron microscope (TEM) Tecnai 20F X-Twin, an electron source, cathode with field emission gun (FEG), EHT = 200 keV, camera for TEM Orius, Gatan Inc.

The X-ray photoelectron spectroscopy (XPS) analysis was carried out to determine the elemental composition, types of functional groups, and chemical bonds on photocatalysts' surface. The samples were measured under high vacuum conditions in the multi-chamber UHV system (Prevac, Poland). Before the analysis, the photocatalysts were immobilized on the molybdenum supports. For X-ray excitation of photoelectrons, a monochromatic Al Kα X-ray radiation (E = 1486.7 eV) was applied. All of the binding energies were calibrated by the C 1 s peak at 285.0 eV.

The Mott Schottky analysis was performed to determine the flat band potential of the TiO_2/Ti_3C_2 composites. The prepared material on fluorine-doped tin oxide glass (FTO) was used as a working electrode tested in a three-electrode system, where Ag/AgCl/0.1 M KCl and Pt mesh were used as reference and counter electrode, respectively. The deaerated 0.5 M Na_2SO_4 solution was used as a supporting electrolyte. The electrochemical spectroscopy impedance (EIS) data were recorded from the anodic towards a cathodic direction. EIS data were recorded for the applied frequency of 1000 Hz in the potential range from 0.1 to −1.2 V vs. Ag/AgCl/0.1 M KCl using a 10 mV amplitude of the AC signal. The potentiostat–galvanostat Biologic SP-150 controlled those conditions. The Mott-Schottky plot describing the relation Csc^{-2} vs. E was obtained using the following calculation of the space charge capacitance $C_{SC} = -1/(2\pi f Z_{im})$, where the imaginary part of the impedance Z_{im} was taken into account, f stands for the frequency of AC signal. The flat band potentials' positions were determined based on the tangent's intersection to the Mott-Schottky plot with the potential (E) axis. The value of donor density was calculated according to the theory of space charge capacitance of the semiconductor given by the relation $N_d = 2/(S \times \varepsilon\varepsilon_0 e)$, where ε is the dielectric constant of TiO_2, ε_0 is the vacuum permittivity, e stays for the electron charge, and S stays for the Mott-Schottky plot. In calculations following values were used: $\varepsilon_0 = 8.85 \times 10^{-12}$F/m, ε = 38 for anatase-$TiO_2$, and $e = 1.602 \times 10^{-19}$C, while S was determined from the run of Mott-Schottky plot.

The photocurrent measurements were carried out in a three-electrode cell, with photocatalyst sample on the FTO glass as the working electrode, Ag|AgCl as the reference electrode, and Pt wire as the counter electrode, in 0.5 M Na_2SO_4 at 20 °C. The electrolyte was purged with argon before the measurements to remove the dissolved oxygen. The photoelectrochemical response was studied in a chronoamperometry measurement at polarization potential of + 0.5 V vs. E_{oc} after the 2000 s of conditioning. Gamry Reference 600+ (Gamry Instruments, USA) potentiostat/galvanostat was used in the experiment.

The Raman spectra were recorded by a confocal micro-Raman spectrometer (InVia Renishaw) with sample excitation using an argon-ion laser emitting at 514 nm and operating at 5% of its total power (50 mW).

Emission spectra and luminescence decay curves were acquired using a grating spectrograph (Princeton Instr. Model Acton 2500i) coupled to a CCD streak camera (Hamamatsu Model C5680) which operates in the 200–1100 nm spectral region with a temporal resolution of 20 ps. As an excitation source, a femtosecond laser (Coherent Model "Libra") coupled to an optical parametric amplifier (Light Conversion Model "OPerA") was used.

The thermogravimetric analysis (TGA) was performed on an SDT 2960 TA analyzer in air atmosphere; heating rate $10° min^{-1}$, under 10 $cm^3 \cdot min^{-1}$ air flow rate, heating range up to 800 °C with powdered samples in a corundum crucible; sample mass 7–10 mg.

Investigation of photocatalyst functional groups before and after irradiation was conducted using Fourier-transform infrared spectroscopy (FTIR). The measurements were carried out using the Nicolet iS10 (Thermo Fisher Scientific Waltham, MA, USA) spectrometer at room temperature. The measurements were conducted in the wavenumber range from 4000 to 400 cm^{-1}.

2.6. Photocatalytic decomposition of phenol – Model organic pollutant

The photocatalytic activity was evaluated in reaction of phenol decomposition under UV–Vis light. The initial concentration of phenol was equal to 20 $mg \cdot dm^{-3}$ (pH = 6.8). The photodegradation reactions were performed in a quartz reactor equipped with an air supply mode. The photocatalyst at the content of 2 $g \cdot dm^{-3}$ and 25 cm^3 of the aqueous solution of the model pollutant (phenol) was introduced into the reactor and kept in the dark for 30 min under continuous stirring to achieve adsorption–desorption equilibrium before irradiation. A 300 W Xe lamp (LOT Oriel, Darmstadt, Germany) was used as an irradiation source. The light flux in the UV range (310 nm < λ < 380 nm) equaled 30 $mW \cdot cm^{-2}$. The sample aliquots were collected at 0, 20, 40, and 60 min of irradiation. The photocatalyst particles were separated from the solution using a 0.2 μm syringe filter. The progress of phenol photodegradation and intermediates concentration were analyzed using reverse-phase high-performance liquid chromatograph Shimadzu LC-6A (Kyoto, Japan) with photodiode array detector Shimadzu SPD-M20A. The measurements were performed at 45 °C and under isocratic flow conditions of 0.3 $cm^3 \cdot min^{-1}$. A volume composition of the mobile phase of 70% acetonitrile, 29.5% water, and 0.5% orthophosphoric acid was applied to determine phenol concentration.

2.7. Photocatalytic decomposition of carbamazepine

In the next step, the TiO_2/Ti_3C_2 and Fe-TiO_2/Ti_3C_2 composites' photocatalytic activity was evaluated in reaction of carbamazepine degradation under UV and UV–Vis light. The initial concentration of carbamazepine was equalled to 14 mg/dm^3 (pH = 6.5). The photocatalytic reactions were performed in the 25 cm^3 quartz reactor equipped with an air supply mode. The photocatalyst at the content of 2 $g \cdot dm^{-3}$ was kept in the dark for 30 min under continuous stirring to achieve adsorption–desorption equilibrium before irradiation. A 300 W

Xe lamp (LOT Oriel, Darmstadt, Germany) was used as an irradiation source. The optical path included a water filter and glass filter UG11 to cut off IR and Vis. The glass filter UG11 transmitted light in the range of 250 ÷ 400 nm (max. 330 nm). The temperature during the experiments was maintained at 20 °C. The sample aliquots were collected at 0, 20, 40, and 60 min of irradiation. Furthermore, the photocatalyst particles were separated from the solution using a 0.2 μm syringe filter. The progress of carbamazepine photodegradation was analyzed using reverse-phase high-performance liquid chromatograph Shimadzu LC-6A (Kyoto, Japan) with photodiode array detector Shimadzu SPD-M20A. The measurements were performed at 45 °C and under isocratic flow conditions of 1.5 $cm^3 \cdot min^{-1}$. A volume composition of the mobile phase of 39.5% acetonitrile, 60% water, and 0.5% orthophosphoric acid was applied to determine carbamazepine concentration.

2.8. Verification of the degradation mechanism using scavengers

The charge carriers and reactive oxygen species participating in the photocatalytic reaction were investigated to provide insight into the mechanism of organic contaminants degradation in the presence of TiO_2/Ti_3C_2 layered composites. The photocatalytic activity was evaluated according to the procedure described in paragraphs 2.4 and 2.5 with the addition of a proper amount of scavenger solution to reach concentrations equal to 20 $mg \cdot dm^{-3}$ and 14 $mg \cdot dm^{-3}$ for phenol and carbamazepine, respectively. EDTA was selected as holes scavenger (h^+), $AgNO_3$ for electrons (e^-), *tert*-butyl alcohol for free hydroxyl radicals (·OH), and benzoquinone for superoxide radical anions ($\cdot O_2^-$).

3. Results and discussion

3.1. Characterization of TiO_2/Ti_3C_2 and Fe-modified TiO_2/Ti_3C_2 photocatalysts

The surface properties of semiconductor material, primarily the surface area, crystallinity, particle size, and exposure of single crystal facets, significantly influenced distinctive physical and chemical properties, including photocatalytic properties in oxidation–reduction reactions.

Fig. 1 shows the TiO_2/Ti_3C_2 composite crystal structure's schematic representation obtained by a two-stage synthesis route. The accordion-like MXene structure was synthesized by selective Al etching from the Ti_3AlC_2-Ti_2AlC matrix. The accordion-like structure of MXene may increase chemical activity and provide unique optical and physicochemical properties arising from the confined thickness and development of the surface area. The surface of MXene was partially oxidized into decahedral anatase particles with exposed {1 0 1} and {0 0 1} facets by the solvothermal reaction in the environment of HBF_4, leading to the formation of the composite structure.

The surface structure determines the efficiency of various groups of pollutants degradation. It also affects the path of their decomposition as a result of differences in (1) the surface density of the excited charge carriers, (2) adsorption capacity of the pollutant, (3) photo-reduction or photo-oxidation properties involving direct pollutants degradation or generation of other reactive oxygen species. Based on our previous study [54], it was assumed that exposed facets are crucial concerning the mineralization efficiency and the pathway of phenol degradation. The TiO_2 octahedral particles exposing {1 0 1} facets favored electron localization on the surface and exhibited the highest phenol mineralization efficiency [54].

The morphological properties were analyzed based on microscopy analysis. The scanning electron microscopy images of TiO_2/Ti_3C_2 composites are shown in Fig. 2 and Fig. 1S in the Supporting Materials. The solvothermal reaction in the presence of HBF_4 aqueous solution led to the oxidation of titanium carbide layers to titanium(IV) oxide. The SEM analysis revealed significant differences between the size of decahedral anatase particles obtained with variable solvothermal reaction time and temperature. An increase in reaction time and temperature caused the formation of smaller, tightly compacted, and differentiated sizes of TiO_2 particles. Furthermore, the reaction performed at the highest temperature of 220°C led to complete oxidation of Ti_3C_2 into the TiO_2 structure. Therefore, for sample TiO_2/Ti_3C_2(220,24) only TiO_2 in the decahedral shape with co-exposed {1 0 1} and {0 0 1} facets was noticed on microscopy images (Fig. 1S and 2S in the Supporting Materials). Exposition of the crystalline planes and surface heterojunction between both facets facilitates inter-facet charge carriers' transport and separation, leading to enhanced photocatalytic activity [55]. Based on scanning microscopy analyzes, co-exposed facets' content was expressed as an average ratio of eight lateral {1 0 1} facets and two vertical {0 0 1} facets, measured for 50 decahedral TiO_2 particles. This value was calculated for two of the most active samples TiO_2/Ti_3C_2(140,12) and TiO_2/Ti_3C_2 (220, 24). The ratio of {1 0 1}/{0 0 1} facets equaled to 45:55. However, due to the agglomeration of anatase decahedral particles, potential exposure of {0 0 1} facets is reduced. According to Yu et al. [56], TiO_2 decahedral particles with the {1 0 1} to {0 0 1} facets ratio equaled to 50:50 possess significantly improved photocatalytic activity. This optimal ratio of facets leads to photogenerated electrons' transfer to {1 0 1} and holes to {0 0 1} facets, hindering the e-h recombination process.

For the most photocatalytic active samples modified with iron species, the TEM analyzes were performed. The SAED pattern of TiO_2/Ti_3C_2(220,24) confirmed the formation of TiO_2. The layer spacing equal to 0.35 nm (Fig. 3-a) referred to (1 0 1) planes found on the exposed {1 0 1} facet of TiO_2. For TiO_2/Ti_3C_2(140,12) composite, two lattice spacings of 0.25 nm and 0.35 nm were also distinguished, indicating the presence of {0 0 6} of Ti_3C_2 and {1 0 1} facet of anatase decahedral particle (Fig. 3-c). The TEM analysis confirmed the presence of Fe at the surface of decahedral anatase particles. Based on the STEM-EDS analysis, the content of iron for Fe-TiO_2/Ti_3C_2(220,24) was about 3 at.%, as shown in Fig. 2S in the Supporting Materials.

The XRD analysis confirmed the presence of 40% of Ti_2AlC and 60% of Ti_3AlC_2 in the MXene precursor – MAX phase. The peaks corresponding to Ti_2CT_x after precursor etching with 48% hydrofluoric acid were not observed, suggesting that Ti_2AlC underwent complete dissolution due to the lower stability compared to Ti_3AlC_2. The XRD patterns of raw Ti_3AlC_2-Ti_2AlC and $Ti_3C_2T_x$ are shown in Fig. 3S in the Supporting Materials. The characteristic reflection attributed to Ti_3AlC_2 at $2\theta = 9.5°$ for the plane (0 0 2) was shifted to a lower value of 8.9° 2θ for

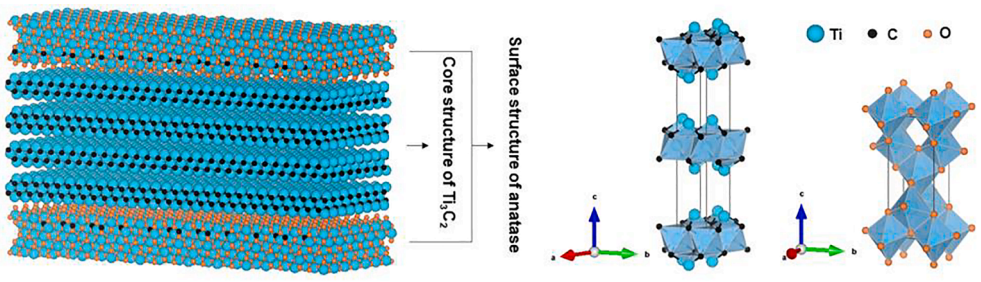

Fig. 1. Visualization of TiO_2-Ti_3C_2 composite crystal structure.

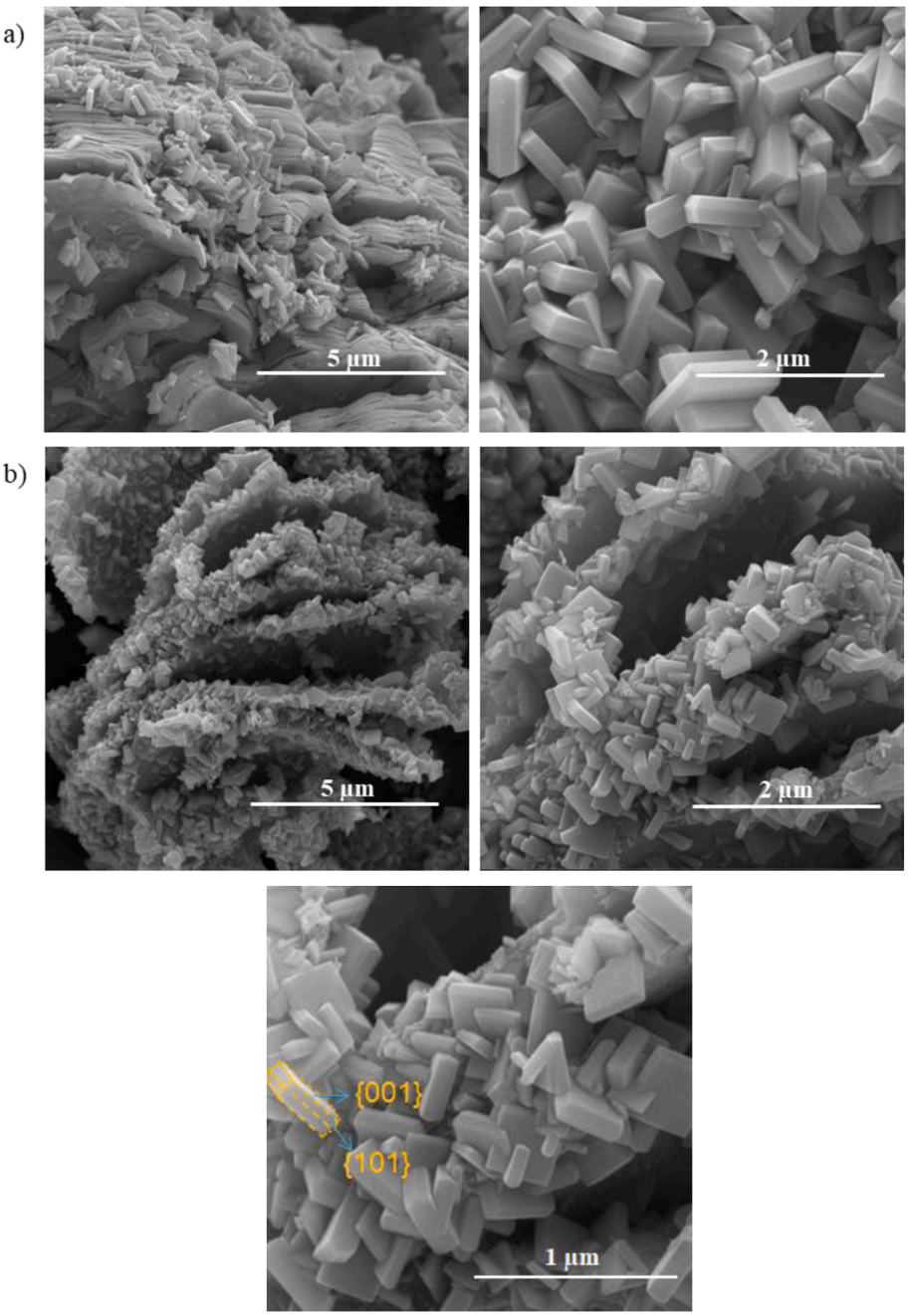

Fig. 2. SEM images of a) TiO_2/Ti_3C_2(160,6) b) TiO_2/Ti_3C_2(140,12).

$Ti_3C_2T_x$. It may be explained as a structural expansion resulting in an increase in *d*-spacing due to the alumina etching from the structure and its substitution with fluoride, oxygen, or hydroxyl terminating groups [57]. The reflection at $2\theta = 25^\circ$ suggesting the presence of a second phase after the etching process using 48% HF, which may be assigned to low quantities of TiO_2 or Al_2O_3. For all the obtained composites, the formation of anatase particles was confirmed. The main diffraction peak of anatase was observed at $2\theta = 25.1^\circ$, corresponding to the (101) plane diffraction, as presented in Fig. 4. Moreover, for anatase particles, the diffraction peak positions attributed to (103), (004), (112), (200), (105), (211), (213), (204), (116), (220), (215), and (301) planes also confirmed the formation of anatase phase, which is in accordance with JCPDS card no. 21–1272. The extension of time and increment of synthesis temperature increased the relative intensity of anatase signals and composites' crystallinity (see Fig. 4 and Table 1S in the Supporting Materials). Furthermore, the reflections specific to Ti_3C_2 at 8.9° 2θ and 18.2° 2θ were observed only for samples TiO_2/Ti_3C_2(140,6), TiO_2/Ti_3C_2(160,6), TiO_2/Ti_3C_2(180,6), TiO_2/Ti_3C_2(140,12). The increase in temperature above 200°C and extended solvothermal reaction time led to oxidation of the $Ti_3C_2T_x$ structure to anatase. Furthermore, signals that occurred at $2\theta = 35.8^\circ$, 41.6°, and 60.4° implied the presence of TiC with crystallite planes (111), (200), and (220), respectively in accordance with JCPDS card no. 65–8417. The diffraction peaks corresponding to lattice plane reflections of iron species should be located at around 25.24°, 35.95°, 36.9°, 47.93°, 54.94°, and 62.0°, but they can be overlapped by peaks attributed to anatase crystallites. Moreover, the presence of iron does not affect the crystal structure of TiO_2/Ti_3C_2 regarding the low amount of Fe loading as well as high dispersion on TiO_2/Ti_3C_2 surface. The intensity of diffraction peaks and anatase crystallite size determined based on the Scherrer equation was similar within the series of samples TiO_2/Ti_3C_2 (140,12), Fe-TiO_2/Ti_3C_2 (140,12), and TiO_2/Ti_3C_2 (220,24), Fe-TiO_2/Ti_3C_2 (220,24) non-

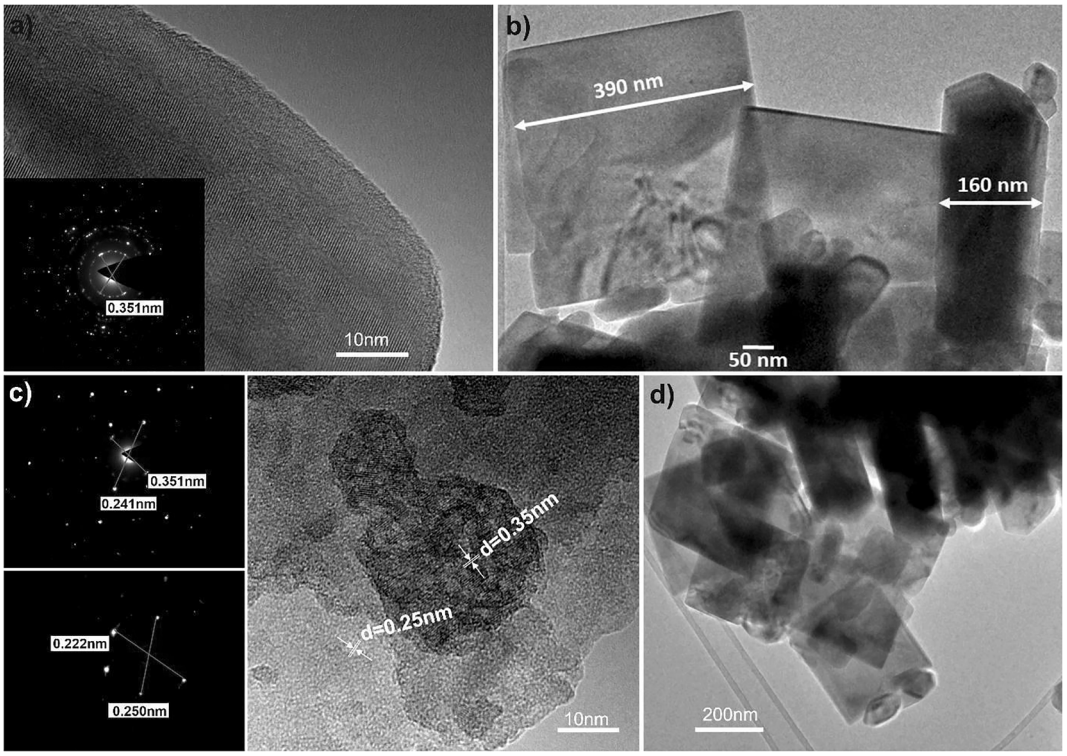

Fig. 3. TEM images and SAED analysis of a) TiO_2/Ti_3C_2(220,24), b) TEM analysis of Fe-TiO_2/Ti_3C_2(220,24), c) SAED and TEM analysis of TiO_2/Ti_3C_2(140,12), d) TEM analysis of Fe-TiO_2/Ti_3C_2(140,12).

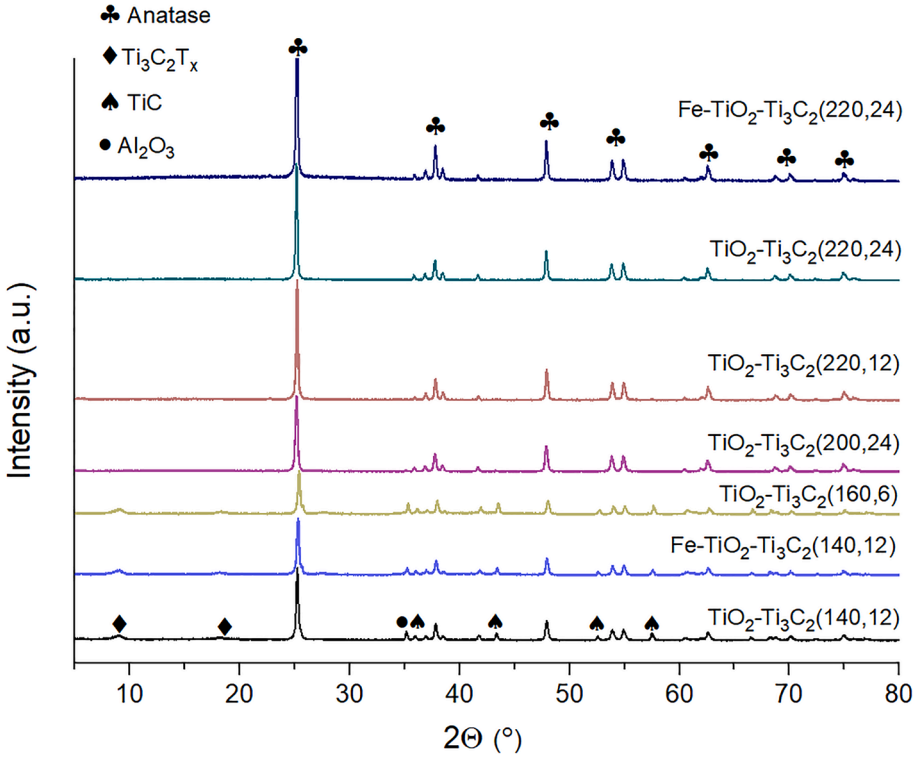

Fig. 4. X-ray diffraction patterns of TiO_2/Ti_3C_2 and Fe-modified TiO_2/Ti_3C_2 composites.

modified and modified with iron (see Table 1).

The TiO_2/Ti_3C_2 photocatalysts' physicochemical properties, e.g., crystallite sizes, indirect band gap values, BET surface areas, are summarized in Table 1. The average anatase crystallite size calculated according to the Scherrer equation varied from about 33 nm to 56 nm for samples TiO_2/Ti_3C_2(200,6) and TiO_2/Ti_3C_2 (140,6), respectively.

The etching of aluminum from Ti_3AlC_2–Ti_2AlC resulted in BET surface area development, which increased 2-fold compared to the raw

Table 1
Characteristics of prepared TiO_2/Ti_3C_2 composites.

No.	Sample	Synthesis conditions		Anatase crystallite size (nm)	BET surface area (m^2/g)	Eg (eV)
		temp. (°C)	time (h)			
1	Ti_3AlC_2-Ti_2AlC	n.d.	n.d.	n.d.	1.7	n.d.
2	$Ti_3C_2T_x$	RT	24	n.d.	3.1	n.d.
3	TiO_2/Ti_3C_2(140,6)	140	6	56	11.4	n.d.
4	TiO_2/Ti_3C_2(140,12)	140	12	36	13.5	n.d.
5	TiO_2/Ti_3C_2(140,24)	140	24	41	6.9	2.4
6	TiO_2/Ti_3C_2(160,6)	160	6	35	10.2	n.d.
7	TiO_2/Ti_3C_2(160,12)	160	12	40	8.0	2.4
8	TiO_2/Ti_3C_2(160,24)	160	24	48	7.1	2.75
9	TiO_2/Ti_3C_2(180,6)	180	6	47	7.6	1.75
10	TiO_2/Ti_3C_2(180,12)	180	12	40	8.2	2.65
11	TiO_2/Ti_3C_2(180,24)	180	24	41	7.0	2.75
12	TiO_2/Ti_3C_2(200,6)	200	6	33.5	6.9	1.85
13	TiO_2/Ti_3C_2(200,12)	200	12	38	7.2	2.75
14	TiO_2/Ti_3C_2(200,24)	200	24	35	5.6	2.95
15	TiO_2/Ti_3C_2(220,6)	220	6	45	5.3	2.5
16	TiO_2/Ti_3C_2(220,12)	220	12	48	6.2	2.75
17	TiO_2/Ti_3C_2(220,24)	220	24	49	5.4	3.0
18	Fe-TiO_2/Ti_3C_2(140,12)	140	12	35	13.9	n.d.
19	Fe-TiO_2/Ti_3C_2(220,24)	220	24	50	5.4	3.0

material of Ti_3AlC_2-Ti_2AlC. For TiO_2/Ti_3C_2 composites, the BET surface area varied from 5.3 to 13.5 $m^2 \cdot g^{-1}$. The formation of TiO_2 on the Ti_3C_2 surface resulted in a 2 to 4-fold increase of the specific surface area. Increasing solvothermal reaction time from 6 to 12 h increased the surface area, while 24-hour reactions had the reverse effect, probably due to the formation of tightly compacted agglomerates of TiO_2 structures. Moreover, an increment of reaction temperature led to a reduction of the photocatalyst's surface area from 13.5 $m^2 \cdot g^{-1}$ to 6.2 $m^2 \cdot g^{-1}$ for samples TiO_2/Ti_3C_2(140,12) synthesized at 140 °C, and TiO_2/Ti_3C_2(220,12) obtained at 220 °C, respectively.

The $Ti_3C_2T_x$ functionalized with -F, -O, and –OH terminate groups after the etching process is a material with metallic properties, showing the characteristic of a narrow bandgap semiconductor (0.05–0.1 eV) [58]. Among TiO_2/Ti_3C_2 composites, only the sample synthesized at the highest temperature of 220 °C for 24 h exhibited the bandgap value comparable with decahedral anatase particles (about 3.0 eV) [59], suggesting complete oxidation of Ti_3C_2 to TiO_2. The narrow bandgap of TiO_2/Ti_3C_2 composites (2.4 eV – 2.75 eV) synthesized at lower temperatures of 140 °C, and 160 °C resulted from a Ti_3C_2 presence in the composite structure, while for samples synthesized in solvothermal reaction for 6–12 h at 200 °C – 220 °C the narrower bandgap resulted from the carbonic species present in the structure of TiO_2 (C-doped TiO_2). The deposition of iron at the TiO_2/Ti_3C_2 sample did not change the physicochemical properties (BET surface area, crystallite size, Eg value) of the obtained composite material.

The XPS was used to determine the surface composition and oxidation state of elements in the TiO_2/Ti_3C_2 composites. The XPS analysis confirmed that samples contain the following elements: Ti, O, C, Al, and F. For TiO_2/Ti_3C_2 composites synthesized from Ti_3AlC_2-Ti_2AlC structure at lower temperatures, the presence of alumina and fluorine in the form of AlF_3 and Al_2O_3 was noticed. As presented in Table 2, aluminum and fluorine content in TiO_2/Ti_3C_2(220,24) was 2.94 at.% and 1.94 at.%, respectively. Moreover, for TiO_2/Ti_3C_2(220,24), higher oxygen and lower carbon content were observed than TiO_2/Ti_3C_2(140,12). These results confirmed the formation of the TiO_2 phase from MXene during the solvothermal reaction at the highest temperature of 220 °C. The surface oxidation of MXene was also confirmed by identifying Ti 2p 1/2 and Ti 2p 3/2 peaks at binding energies of 465 eV and 459 eV, which corresponds to Ti^{4+} in TiO_2 structure.

The XPS spectra for high-resolution Ti 2p, O 1 s, C 1 s core levels of TiO_2/Ti_3C_2 composites are presented in Fig. 5. Besides the most intense signal at 459 eV from the Ti-O bond, the Ti 2p3/2 region could be deconvoluted for components centered at 454.8 eV, 455.4 eV, 456.1 eV, 456.8 eV, 458 eV corresponding to Ti-C and C-Ti-O bonds. Similar to research performed by Shen et al. [60], the XPS analysis revealed the presence of C-Ti-F bonds with a signal located at 460.5 eV.

Typical binding energy at about 530.5 eV was related to oxygen in the TiO_2 crystal lattice (Ti–O–Ti). According to Peng et al. [61], the peak at 531.3 eV was assigned to oxygen in Ti–OH/C = O bonds and the peak at 532.3 eV was related to oxygen in the C–OH bonds. Further signals located at 533.2 eV and 534 eV may be attributed to Al_2O_3 and adsorbed water, respectively [62].

The C 1 s region could be deconvoluted for five peaks at 281.9 eV, 283.3 eV, 284.3 eV, 285 eV, 285.6 eV, which can be assigned to Ti-C, C-Ti-O bonding at the interfaces of TiO_2/Ti_3C_2, C = C (sp2), C–C (sp3), C–H (sp3), respectively [63]. Meanwhile, signals at 286.4 eV, 287.2 eV, 289.3 eV correspond to C-OH, C-O-C, and O = C-OH [64]. The Ti-C, C-Ti-O bonds were observed for sample TiO_2/Ti_3C_2(140,12) synthesized at a lower temperature of the solvothermal reaction, while for TiO_2/Ti_3C_2(220,24) were not observed due to complete oxidation of Ti_3C_2 to TiO_2.

The surface properties of photocatalyst modified with iron were similar to pure TiO_2/Ti_3C_2 samples. Meanwhile, the XPS analysis confirmed the presence of 0.7 at.% of iron after magnetron sputtering at sample TiO_2/Ti_3C_2(220,24) and 0.67 at.% of iron for TiO_2/Ti_3C_2(140,12). For Fe-modified TiO_2/Ti_3C_2 photocatalyst broad Fe 2p 3/2 peak with multiplet splitting characteristic for iron oxides was observed, as presented in Fig. 6. The XPS spectrum of Fe 2p can be resolved in two main peaks, which are ascribed to FeO at 711.5 eV and Fe_2O_3 at 712 eV.

The DR/UV–Vis absorption spectra of TiO_2/Ti_3C_2 and Fe-TiO_2/Ti_3C_2 composites are shown in Fig. 7. The TiO_2/Ti_3C_2 composites absorbed both UV and visible light. The threshold around 400 nm was observed on the spectra, indicating the formation of titanium(IV) oxide on the MXene surface. Moreover, the nanocomposites obtained at higher temperatures (200 °C and 220 °C) and with a longer reaction time (12 h or 24 h) were characterized with lower light absorption in the range of 400–800 nm than those obtained at 140 °C and 160 °C. A decrease in visible light absorption and emergence of absorption shoulder with a threshold at 400 nm is correlated with the formation of the TiO_2 phase. The deposition of iron on TiO_2/Ti_3C_2 did not change the shape of spectra and absorption intensity. Compared to TiO_2/Ti_3C_2(220,24) sample containing decahedral anatase particles, higher absorption properties for

Table 2
XPS analysis of Ti, O, C, Al, F content (at.%) for the selected composites TiO_2-Ti_3C_2(140,12) ,TiO_2-Ti_3C_2 (220,24), and Fe-TiO_2-Ti_3C_2(220,24).

Sample	Content (at.%)						
	C 1 s	N 1 s	O 1 s	F 1 s	Al 2p	Ti 2p	Fe 2p
TiO_2/Ti_3C_2(140,12)	24.69	1.03	41.47	6.02	9.01	17.78	–
TiO_2/Ti_3C_2(220,24)	33.50	0.48	43.65	1.69	2.94	17.74	–
Fe-TiO_2/Ti_3C_2(220,24)	26.2	–	51.6	1.1	–	20.5	0.7

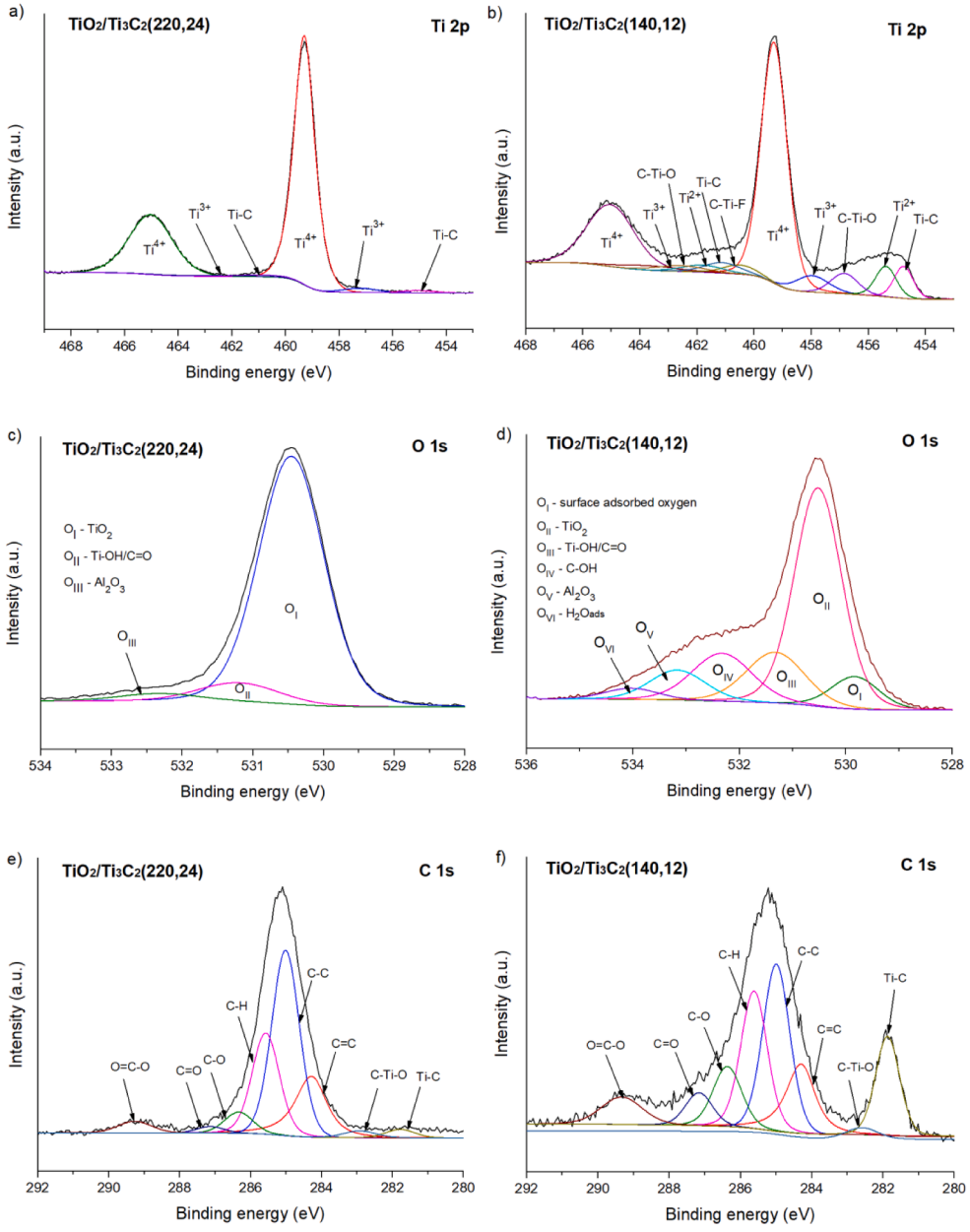

Fig. 5. XPS spectra of titanium (Ti 2p), oxygen (O 1 s), and carbon (C 1 s) region for samples TiO_2/Ti_3C_2(220,24) and TiO_2/Ti_3C_2(140,12).

Fe-modified TiO_2/Ti_3C_2(220,24) sample were observed in the Vis light range of 400–500 nm. Xu et al. [65] reported that the absorption edge for pristine TiO_2 was increased in the visible light region from 390 to 750 nm after ultra-thin Fe_2O_3 surface modification.

The Raman spectra measured for selected photocatalysts presented in Fig. 8 consist of typical anatase active modes [66]. Their detailed interpretation is provided in Table 3. However, it should be underlined that typically the Eg(1) band is observed at 144 cm^{-1} while the maxima were placed at 150 cm^{-1}. Such a blue shift can result from a much smaller grain size (phonon confinement effect) compared to the literature ones or surface coating [67]. The spectra are quite similar in the range from 100 cm^{-1} to 1200 cm^{-1}, and their intensity increased with TiO_2 content. The surface compound can induce some comprehensive stress on the most outer atoms of titanium, and following that, the change in Eg(1) position occurs. Indeed, in most cases, signals typical for carbonaceous species can be easily detected, known as D and G bands [68]. The first one, located at ca. 1363 cm^{-1}, is a breathing mode of A1g symmetry, including phonons near the K zone boundary and originating from the structural defects in the carbon lattice. The G-band present at ca. 1584 cm^{-1} is assigned to the in-plane vibrations of sp^2 carbon atoms and is a doubly degenerated phonon mode (E2g) at the Brillouin zone center. Those features confirm that carbon forms exhibit graphitic character and can also be responsible for the Eg(1) mode shift.

The EPR spectra are presented in Fig. 9 as the signal intensity against the G value. The Lande factor (G) was calculated according to the equation:

$$G = \frac{h\hat{A}\cdot f}{m_B\hat{A}\cdot B} \quad (1)$$

where: G–Lande factor (a.u.); h–Planck's constant ($6.62\cdot10^{-34}$; J·s); f–frequency (Hz); mB–Bohr magneton ($9.2740154\cdot10^{-24}$; $J\cdot T^{-1}$); and B–magnetic field induction (T).

The characteristic G values of about 1.995–2.0 correspond to oxygen (v_o) or carbon vacancies (v_c) and of about 1.94 to the presence of Ti^{3+}, which may have originated from Ti_3C_2. For TiO_2/Ti_3C_2 layered composites, the recorded EPR resonances line was broad and unresolved,

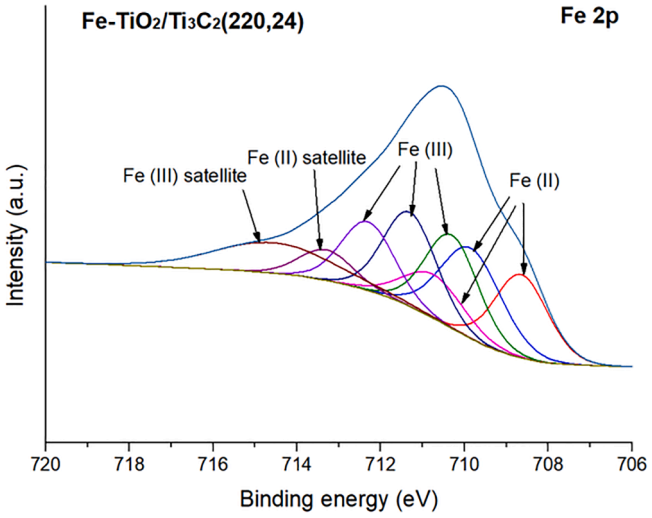

Fig. 6. XPS spectrum of iron (Fe 2p) region for sample Fe-TiO_2/Ti_3C_2.

which demonstrates the formation of a high number of defects [69]. The highest resonance line about g = 1.94 was noticed for the TiO_2/Ti_3C_2(140,12) sample, suggesting a higher concentration of Ti^{3+}. Meanwhile, for the sample TiO_2/Ti_3C_2(220,24), the strongest signal occurred about g = 2.0 and may be assigned to the oxygen or carbon vacancies. Zhang et al. [70] reported that the formation of carbon vacancies, which exposed a large number of active sites, may inhibit the electron-hole recombination process and thus lead to higher photocatalytic activity. Moreover, Shen et al. [60] observed that v_c promotes pollutants adsorption on the photocatalyst surface, modulates the electronic structure, and improves charge carriers accumulation. Carbon vacancies with unpaired electrons represent conversion centers, where photo-generated electrons may absorb oxygen for the generation of photocatalytic active species, e.g., superoxide anion radicals ($\cdot O_2^-$) [71–72]. The active sites – Ti^{3+} species and carbon vacancies may participate in the contaminants' adsorption on the photocatalyst surface. Furthermore, they represent trapping sites for the photo-formed conduction band electrons [73]. Xu et al. [74] proved that the existence of Ti^{3+} defects enhances visible-light-driven photocatalysis due to bandgap narrowing.

The emission spectra of the most photocatalytic active TiO_2/Ti_3C_2 and Fe-TiO_2/Ti_3C_2 composites were measured under 350 nm excitation at room temperature, and the results are presented in Fig. 10. For all compounds, the broad band in the blue region was observed. For samples TiO_2/Ti_3C_2(140,12) and Fe-TiO_2/Ti_3C_2(140,12) synthesized at 140 °C, the peak maximum was about 460 nm, while for TiO_2/Ti_3C_2(220,24) and Fe-TiO_2/Ti_3C_2(220,24) samples obtained at a higher temperature of 220 °C the peak was shifted to 470 nm. As the emission spectra strongly depend on the particles surrounding the environment [75], it may suggest that higher synthesis temperature leads to the changes of the photocatalyst surface. The emission of the composites was similar to the luminescence of anatase (TiO_2) [76] and can be assigned to charge transfer transition from Ti^{4+} to O^- at the sites near defects [77] and emission from the surface oxygen vacancies or defects [78]. The blue shift observed for presented photocatalysts may also be the result of the Burstein-Moss effect. The effect is even more expected as the Fe-modified samples are slightly more blue-shifted compared to unmodified samples. It is also important to notice that time and laser power may also lead to the bathochromic effect [79].

The decay curves of the composites' luminescence were registered under 350 fs pulse laser at room temperature. It can be noted that the decay profiles showed the non-exponential character. The non-exponential profiles of luminescence decays suggest the existence of carrier trapping sites with different energy levels, leading to a distribution of the carrier transport rates [77]. To calculate decays for all samples, two-phase exponential decay function with time constant parameters were used:

$$y = y_0 + A_1 e^{-x/t_1} + A_2 e^{-x/t_2}$$

The analysis of the decay curves showed that longer time and higher synthesis temperature led to shortening of the luminescence lifetimes (see Fig. 11). This may suggest a decrease in the number of luminescent centers (defects) after a more prolonged synthesis at the higher temperature. Analysis of the luminescence decay time showed that Fe-modified samples revealed longer decays, suggesting energy transfer between TiO_2 and Fe species.

As presented in Fig. 12, the Mott Schottky plots' positive slope demonstrated the n-type semiconductivity characteristic of TiO_2/Ti_3C_2 composites [80]. According to Xu et al. [81], regions 1, 2, and 3 correspond to the potential ranges in which the capacitance is dominated by the FTO substrate FTO/layer interface and the semiconducting

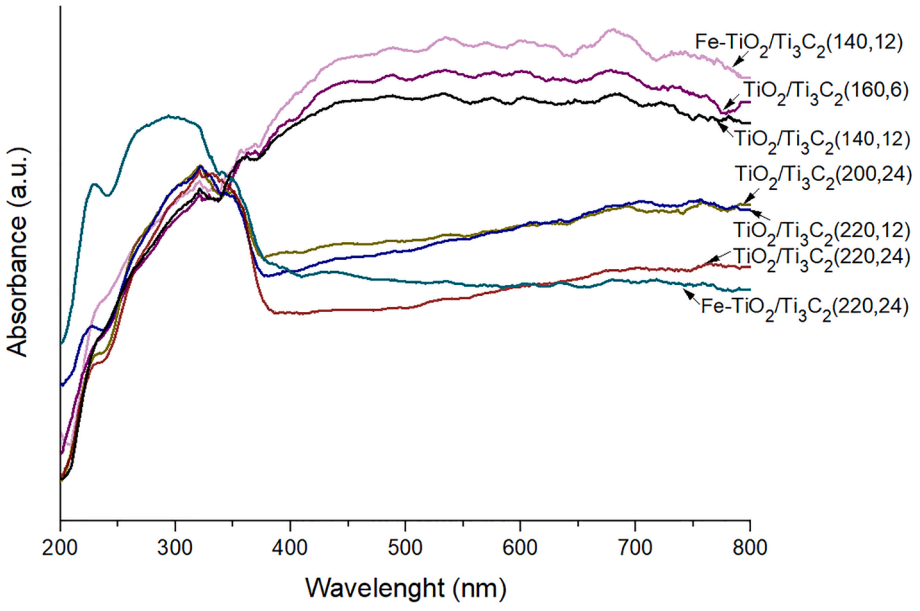

Fig. 7. DR/UV–Vis spectra of the selected TiO_2/Ti_3C_2 and Fe-TiO_2/Ti_3C_2 composites.

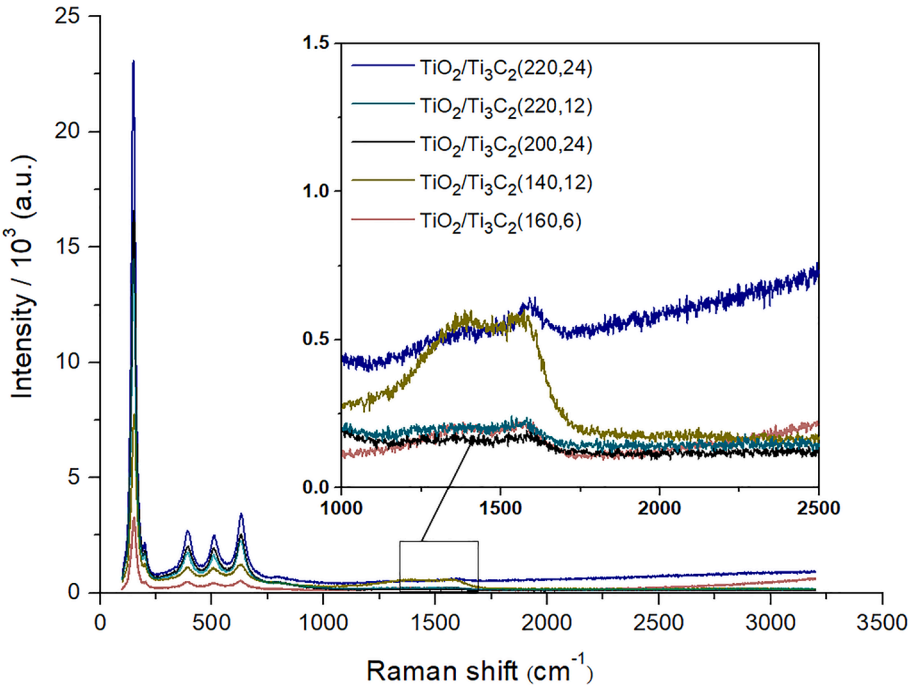

Fig. 8. Raman spectra of selected TiO_2/Ti_3C_2 composites.

Table 3
Wavenumbers of the samples with their assignment.

Band localization (cm^{-1})	Assignment
150	Eg(1)
200	Eg(2)
395	B1g(1)
512	Double signal of B1g(2) and A1g
633	Eg(3)
805	First overtone of B1g at 395 cm^{-1}
1363	D band
1584	G band

film deposited onto FTO. A similar shape of the Mott-Schottky plot was recorded by Bresolin et al. [82] and described by Bisquert [83]. When the applied potential fits the 1st and 2nd region, the space charge zone is depleted, and the capacitances of the tested electrodes are similar and overlap this of bare FTO substrate. A linear fit, indicated by the grey arrow, provides an E_{fb} of very similar value: ca. −0.3 V vs. Ag/AgCl/0.1 M KCl attributed to the FTO-dominated response. In a more cathodic range, the activity of all tested materials differs significantly, and the second flat band potential value can be distinguished, see Table 4. According to the provided data, the FTO/TiO_2/Ti_3C_2(140,12) exhibits the most positive E_{fb2} value comparing to bare FTO, FTO/ TiO_2/ Ti_3C_2(140,24), and FTO/TiO_2/Ti_3C_2(220,24). For iron-modified Ti_3C_2,

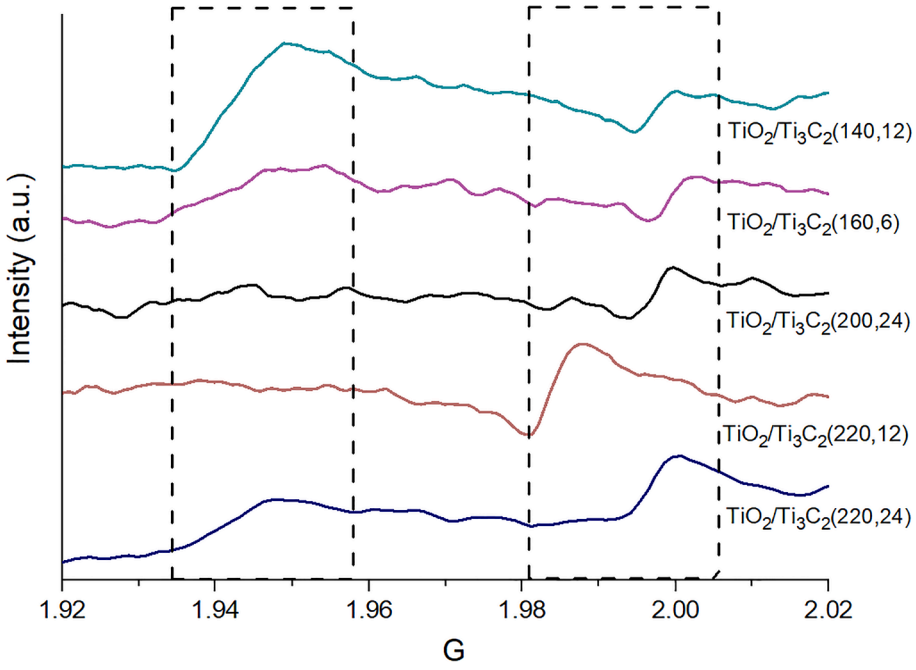

Fig. 9. The EPR spectra recorded at RT for selected TiO_2/Ti_3C_2 composites.

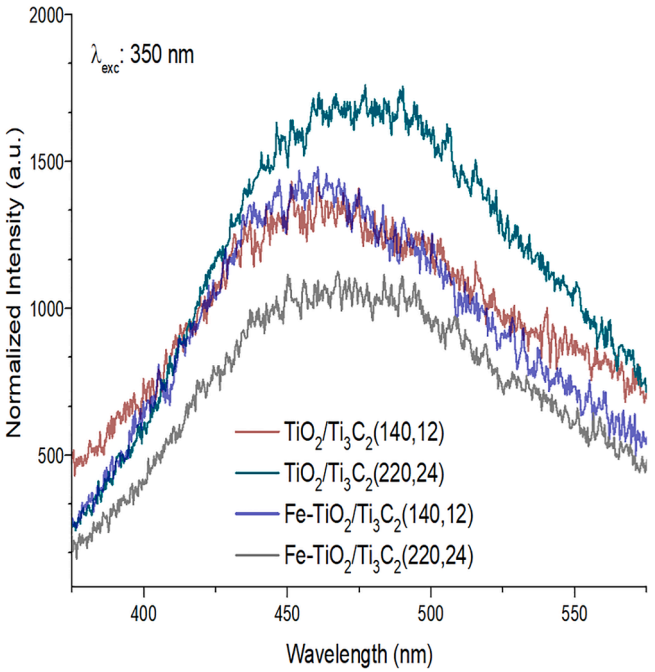

Fig. 10. Photoluminescence emission spectra of TiO_2/Ti_3C_2 and Fe-TiO_2/Ti_3C_2 photocatalysts.

only one value of flat band potential can be determined, indicating the high impact of the Fe presence on the electrochemical activity.

For n-type semiconductors, the flat band potential is almost equal to the conduction band potential. Thus, according to values of E_{fb} and E_g, the valence band (VB) edge of composites may be determined by the following equation:

$$E_{VB} = E_g + E_{CB}$$

The calculated valence band positions of TiO_2/Ti_3C_2(140,24), TiO_2/Ti_3C_2(220,24) and TiO_2/Ti_3C_2(140,12) are approximately 1.53 eV, 2.25 eV and 2.21 eV, respectively. A more positive location of VB is associated with stronger oxidation power. Thus, samples TiO_2/Ti_3C_2(220,24) and TiO_2/Ti_3C_2(140,12) exhibited enhance photocatalytic activity towards degradation of phenol and carbamazepine compared to TiO_2/Ti_3C_2(140,24).

The Mott-Schottky analysis indicated a significant increment in donor density accompanied by a positive shift of flat band potential of Fe-modified TiO_2/Ti_3C_2 samples comparing to neat TiO_2/Ti_3C_2, which is recognized to be a key factor responsible for photocatalytic oxidation reactions.

The electrochemical impedance spectroscopy Nyquist plots of the most photocatalytic active TiO_2/Ti_3C_2 and Fe-TiO_2/Ti_3C_2 photocatalysts recorded in the dark and under UV–Vis irradiation at polarization potential of + 0.5 V vs. E_{oc} are shown in Fig. 4S. a). The arc radius of iron-modified TiO_2/Ti_3C_2 in the EIS Nyquist plot was lower than unmodified TiO_2/Ti_3C_2 composites indicating improved charge carriers separation. Furthermore, the smallest arc radius was recorded for sample Fe-TiO_2/Ti_3C_2(220,24). These results indicate a larger electroactive surface area and low charge transfer resistance, implying an effective separation of the photo-generated electron-hole pairs [84].

The photocurrent response of TiO_2/Ti_3C_2 and Fe-TiO_2/Ti_3C_2 upon on–off cycles of UV–Vis light irradiation is presented in Fig. 4S b) in the Supporting Materials. For all samples, the photocurrent increases when light is switched on and decreases when the light off, indicating that the materials respond to light with good reproducibility. Furthermore, photocurrent responses maintain superior stability after ten on/off cycles, which indicates that the photocatalyst may restrain photocorrosion [85]. According to the literature, $Ti_3C_2T_x$, which acts as a metallic conductor exhibits minimal, nearly no photocurrent generation [86–88]. Photo-generated electrons in the TiO_2/Ti_3C_2 originate from TiO_2, while Ti_3C_2 is involved in the electron transfer [89]. Thus the lowest photocurrent was observed for sample TiO_2/Ti_3C_2(140,12), characterized by lower TiO_2 content. Higher photocurrent means lower recombination of photo-generated electrons and holes, higher photoelectron transfer efficiency, and more light absorbance.

Furthermore, it can be observed in absorption spectra (Fig. 7) that TiO_2/Ti_3C_2(220,24) composite have much higher absorption in the UV range what may be another proof of the generation of new v_O vacancy band locating just below the conduction band edge of pure TiO_2. The high concentration of v_o defects may lead to much higher UV light-induced photoelectron generation [90] compared to the rest of the

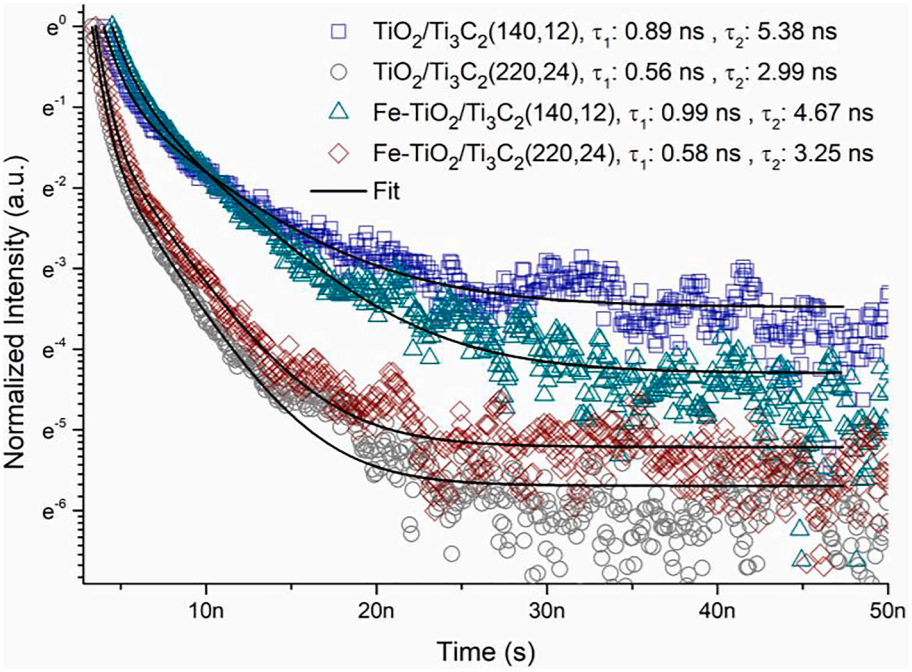

Fig. 11. Time-resolved photoluminescence decay spectra of TiO_2/Ti_3C_2 and Fe-TiO_2/Ti_3C_2 photocatalysts.

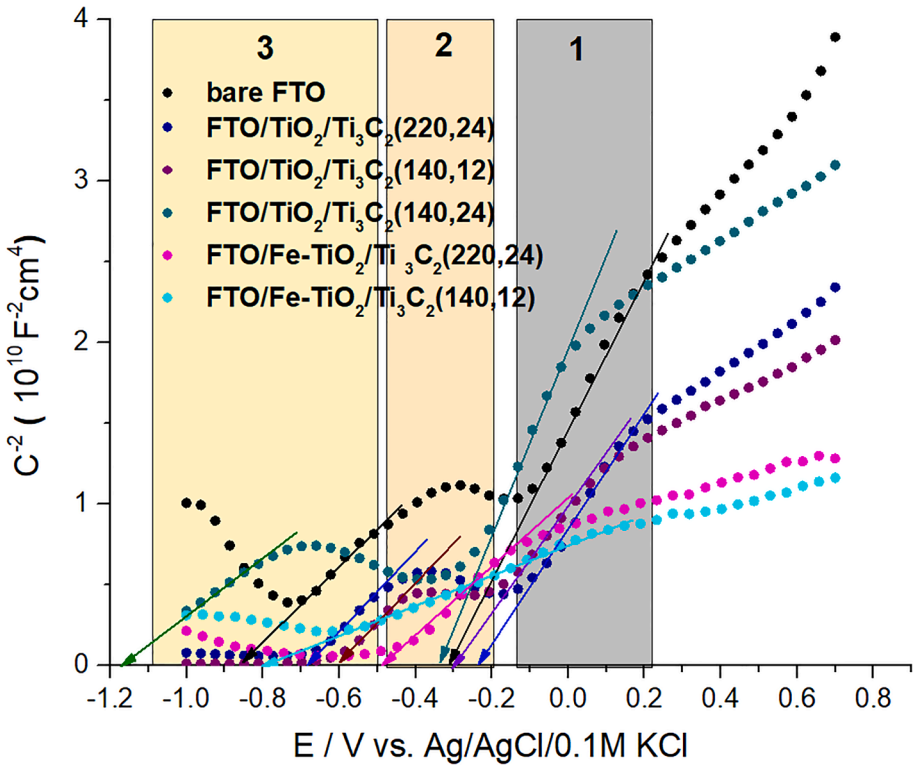

Fig. 12. Mott-Schottky plots for bare FTO and coated with samples TiO_2/Ti_3C_2(140,12), TiO_2/Ti_3C_2(140,24), TiO_2/Ti_3C_2(220,24), Fe-TiO_2/Ti_3C_2(140,12) and $FeTiO_2/Ti_3C_2$(220,24).

Table 4
The value of flat band potential and donor density determined for tested photocatalytic materials.

Sample	E_{fb1}	E_{fb2}	slope / $10^{10}F^{-2}cm^4/V$	N_d / 10^{20} cm^{-3}
Bare FTO	−0.31	−0.94	–	–
FTO/ TiO_2/ Ti_3C_2(220,24)	−0.25	−0.69	2.25	1.65
FTO/ TiO_2/ Ti_3C_2(140,12)	−0.29	−0.60	2.21	1.68
FTO/ TiO_2/ Ti_3C_2(140,24)	−0.33	−1.15	1.53	2.43
FTO/ Fe-TiO_2/ Ti_3C_2(220,24)	–	−0.80	2.12	1.75
FTO/Fe-TiO_2/ Ti_3C_2(140,12)	–	−0.49	1.91	4.05

composites. Also, EPR spectra (Fig. 9) showed a strong signal at a g-value of 2.00, indicating the significant presence of v_o. This signal can be caused by electrons trapped on surface vacancies v_o [91]. A similar effect was observed by Bao et al. [86] for TiO_2/Ti_3C_2 composites obtained by calcination of Ti_3C_2 under air condition at 350, 450, 550, and 650°C, respectively. The highest photocurrent was recorded for a sample calcined at 550°C.

Additionally, the highest value of photocurrent (~0.4 μA/cm^2) was produced for the sample TiO_2/Ti_3C_2(220,24) modified with iron compared to un-modified material (~0.25 μA/cm^2). These results confirmed that Fe-modification positively influences the photocurrent values, thus indicating a more efficient separation of the photoexcited electron-hole pairs. It can also be observed that samples modified with iron species showed slower decay, indicating long charge carrier lifetimes and metastable donor states (also noticed in photoluminescence measurements).

Thermogravimetric analyzes were conducted for two of the most active TiO_2/Ti_3C_2 composites, as presented in Fig. 5S in the Supporting Materials. The thermal decomposition involved two exothermic steps. The first step with a weight loss of 0.15% in the range of 25–287 °C and 0.28% in the range of 25–235 °C. The second step with a weight loss of 1.73 in the range of 287–646 and 0.98% in the range of 235–581 °C. TGA measurements indicated the thermal stability of the compounds heated in an oxygen-rich atmosphere. It was proved by the total weight loss of 1.88% for the TiO_2/Ti_3C_2(140,12) and 1.26% for the TiO_2/Ti_3C_2(220, 24) sample.

To study the TiO_2/Ti_3C_2 photocatalysts' surface properties, the electrophoretic mobility of these photocatalysts at different pH values was investigated. The zeta potential was positive at lower pH and negative at higher pH values, as presented in Fig. 6S in the Supporting Materials. The isoelectric point (IEP) was observed at pH = 3.6 and pH = 4.7 for TiO_2/Ti_3C_2(140,12) and TiO_2/Ti_3C_2(220,24), respectively. It can be observed that the isoelectric point for TiO_2/Ti_3C_2(140,12) is shifted toward a lower pH value in comparison to the TiO_2/Ti_3C_2(220,24) sample. According to the literature, IEP for anatase TiO_2 is observed at a pH of 6 [92]. A decrease in IEP value may be attributed to the presence of MXenes, which are negatively charged. The zeta potential of an aqueous suspension of $Ti_3C_2T_X$ nanosheets was equaled to −34.75 mV [93]. Moreover, according to Kosmulski et al.[94] the presence of carbonates on the surface induces a shift in the IEP to lower pH values. The pH of carbamazepine solution during the photodegradation tests was set at 6.5. Thus, carbamazepine was primarily in the protonated form ($pH < K_{a,\ CBZ}$). As a weak acid with pKa equal to 10, phenol was present in the solution with a pH of 6.8, mainly in the molecular form. At these conditions, the Ti_3C_2 photocatalyst's surface was negatively charged, and the values of zeta potential were below −40 mV. Thus, the suspensions of all tested TiO_2/Ti_3C_2 and Fe-TiO_2/Ti_3C_2 particles were stable and did not agglomerate during the photocatalytic reaction.

3.2. Photocatalytic activity in reaction of phenol and carbamazepine degradation

The TiO_2/Ti_3C_2 composites' photocatalytic activity was studied in the photodegradation reaction of phenol as a model organic pollutant and carbamazepine belonging to the group of emerging contaminants not-susceptible to biodegradation. The results of photodegradation are presented in Table 5. The phenol decomposition efficiency ranged from 19 to 69% within 60 min of irradiation. The obtained results confirmed the crucial role of formed titanium(IV) oxide on organic compounds' oxidation efficiency.

The lowest phenol degradation rate constant ($k = 0.3 \pm 0.2 \cdot 10^{-2}$ min^{-1}) was observed for TiO_2/Ti_3C_2(140,6), which resulted from the minimal quantity of TiO_2 formed on the MXene surface. The highest photocatalytic activity was noticed for samples TiO_2/Ti_3C_2(160,6), TiO_2/Ti_3C_2(220,12), and TiO_2/Ti_3C_2(220,24) with the degradation rate constants equal to $1.8 \pm 0.05 \cdot 10^{-2}$ min^{-1}, $1.7 \pm 0.04 \cdot 10^{-2}$ min^{-1}, and $1.9 \pm 0.03 \cdot 10^{-2}$ min^{-1}, respectively. The higher the temperature and longer hydrothermal treatment time, the higher the photocatalytic activity. In this case, an increase of the TiO_2 content and crystallinity by prolonging solvothermal reaction time resulted in a more efficient generation of electrons and holes. The formation of surface heterojunction between {101} and {001} facets of decahedral anatase particles grown on Ti_3C_2 surface led to improved photoelectron transfer, which reduced charge carriers recombination. Except for the TiO_2/Ti_3C_2(220,12), TiO_2/Ti_3C_2(220,24), TiO_2/Ti_3C_2 (160,6), and TiO_2/Ti_3C_2(140,12) samples, containing titanium vacancies (Ti^{3+} centers) and oxygen or carbon vacancies at the surface, for other obtained TiO_2/Ti_3C_2 composite photocatalysts, the degradation rate constant fluctuated from 0.5 to $0.8 \cdot 10^{-2}$ min^{-1}. In all photodegradation processes, *ortho*-hydroxyphenol and *para*-hydroxyphenol were detected as the first intermediates of phenol decomposition, see Fig. 13.

The phenol degradation mainly proceeds by the attack of hydroxyl radicals on the phenyl ring, leading to *para*-hydroxyphenol and ortho-hydroxyphenol formation. For the TiO_2/Ti_3C_2(140,12) sample containing V_{Ti}, a higher concentration of *para*-hydroxyphenol than *ortho*-hydroxyphenol was noticed. In this case, electrons are accumulated on the surface (Ti^{3+} states), preventing h^+ location on the surface oxygen and further H_2O molecule oxidation to ·OH radicals. For TiO_2/Ti_3C_2(220,24) higher concentration of *ortho*-hydroxyphenol compared to sample TiO_2/Ti_3C_2(140,12) was observed. Different amounts of electrons and holes resulted in different abilities in forming ·OH, which are crucial reactive oxygen species in phenol photocatalytic decomposition.

The five samples with the highest activity in phenol decomposition were selected for evaluation of photocatalytic carbamazepine removal. The highest activity was observed for sample TiO_2/Ti_3C_2(140,12) with 96% degradation after 60 min of irradiation ($k = 5.2 \cdot 10^{-2}$ min^{-1}).

As presented in Fig. 14, the overall activity was higher than those observed for phenol decomposition. The differences in photodegradation efficiency resulted from differences in HOMO energy for phenol and carbamazepine. Higher HOMO energy (more positive value) of the decomposed compound makes it more susceptible to oxidation. According to the literature, HOMO energy calculated using the B3LYP/6–311++G method is equal to about −0.30 eV for carbamazepine [95], while for phenol −5.95 eV [96].

Shahzad et al. [97] have also reported the degradation of carbamazepine in the presence of $TiO_2/Ti_3C_2T_x$ composite with exposed {001} facets. However, the kinetic of carbamazepine degradation was slow. After 8 h of irradiation in the presence of simulated solar light, only 55% of the total carbamazepine was degraded, while in UV light, after 3 h of irradiation, almost 99% of CBZ was removed. The major detected intermediates of CBZ photodegradation were acridine, 2-aminobenzoic acid, 2-hydroxybenzoic acid, and formaldehyde-acridine [94].

In this study, formation of {001} and {101} facets in TiO_2/Ti_3C_2 layered composite markedly improved photocatalytic activity due to a surface heterojunction between {001} and {101} facets of TiO_2. After 1 h of UV–Vis light irradiation, more than 90% of carbamazepine was degraded. The co-exposed facets led to a more efficient transfer of photo-induced charge carriers. The CB and VB of {001} facets are located slightly higher than for {101} facets. It leads to the accumulation of photogenerated electrons on the {101} and holes on the {001} facets.

Moreover, modification of TiO_2/Ti_3C_2(140,12) surface with iron species resulted in complete carbamazepine degradation after 1 h of UV–Vis light irradiation with the degradation rate constant equal to $8.8 \pm 0.11 \cdot 10^{-2}$ min^{-1}, as presented in Fig. 15. The degradation efficiency for Fe-modified TiO_2/Ti_3C_2 was higher in UV–Vis than in UV light, confirming the effect of iron modification on TiO_2/Ti_3C_2 enhanced photocatalytic activity (see in Fig. 7S in the Supporting Materials). Iron oxides may increase the photocatalytic efficiency of TiO_2, as Fe ions can enact as hole and electron scavengers, thus inhibiting the recombination of the photo-generated charge carriers. Similar results were reported by Tada et al. [98] for the decomposition of 2-naphthol in the presence of surface-modified TiO_2 with highly dispersed iron oxide nanoparticles. Iron oxide-modified TiO_2 exhibited significantly higher photocatalytic activity under UV–Vis light irradiation.

For all investigated composites, hydroxycarbamazepine and small quantities of acridine were distinguished as intermediate products. The increased amount of acridine could be an indicator of the limiting step since acridine ultimately led to the formation of a stable molecule of acridone [99]. Hydroxy-carbamazepine is the first possible product of CBZ oxidation, and therefore, acts as a substrate for further oxidation. These results illustrate well intensification of the process of CBZ photocatalytic degradation.

The TiO_2/Ti_3C_2(140,12) photocatalyst and Fe-TiO_2/Ti_3C_2(140,12)

Table 5
The rate constant of phenol and carbamazepine degradation in the presence of TiO_2, TiO_2/Ti_3C_2, and Fe-TiO_2/Ti_3C_2 samples.

No.	Sample label	Phenol degradation rate constant($min^{-1} \cdot 10^{-2}$)	Carbamazepine degradation rate constant($min^{-1} \cdot 10^{-2}$)
1	TiO_2/Ti_3C_2(140,6)	0.30 ± 0.2	n.d.
2	TiO_2/Ti_3C_2(140,12)	1.05 ± 0.07	5.20 ± 0.11
3	TiO_2/Ti_3C_2(140,24)	0.60 ± 0.05	n.d.
4	TiO_2/Ti_3C_2(160,6)	1.80 ± 0.05	2.40 ± 0.15
5	TiO_2/Ti_3C_2(160,12)	0.70 ± 0.02	n.d.
6	TiO_2/Ti_3C_2(160,24)	0.70 ± 0.01	n.d.
7	TiO_2/Ti_3C_2(180,6)	0.50 ± 0.01	n.d.
8	TiO_2/Ti_3C_2(180,12)	0.70 ± 0.03	n.d.
9	TiO_2/Ti_3C_2(180,24)	0.80 ± 0.05	n.d.
10	TiO_2/Ti_3C_2(200,6)	0.70 ± 0.01	n.d.
11	TiO_2/Ti_3C_2(200,12)	0.70 ± 0.03	n.d.
12	TiO_2/Ti_3C_2(200,24)	1.60 ± 0.02	2.50 ± 0.09
13	TiO_2/Ti_3C_2(220,6)	0.70 ± 0.03	n.d.
14	TiO_2/Ti_3C_2(220,12)	1.70 ± 0.04	3.10 ± 0.16
15	TiO_2/Ti_3C_2(220,24)	1.90 ± 0.03	3.90 ± 0.14
16	Fe-TiO_2/Ti_3C_2(140,12)	n.d.	8.80 ± 0.11
17	Fe-TiO_2/Ti_3C_2(220,24)	n.d.	5.60 ± 0.07

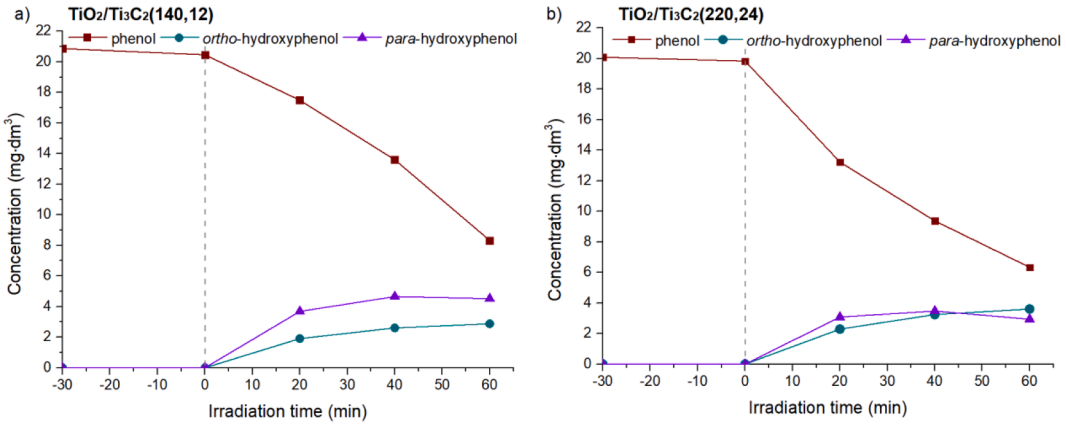

Fig. 13. Mean concentration change curves for exemplary samples TiO_2/Ti_3C_2(140,12) and TiO_2/Ti_3C_2(220,24) during phenol degradation. Detailed results for each sample are presented in Table 2S in the Supporting Materials.

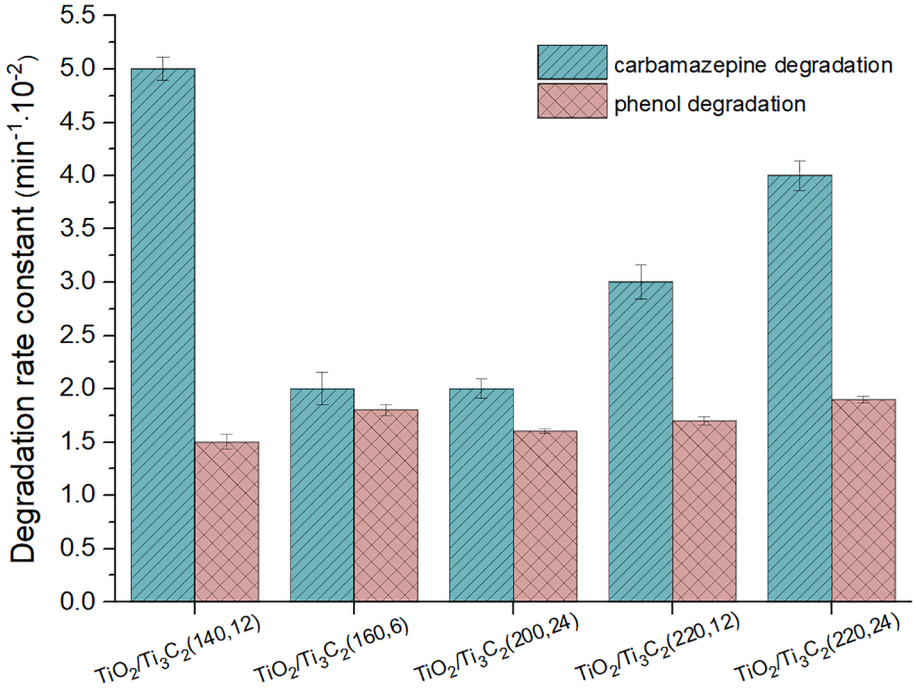

Fig. 14. Phenol and carbamazepine removal rate constant for selected TiO_2/Ti_3C_2 composites.

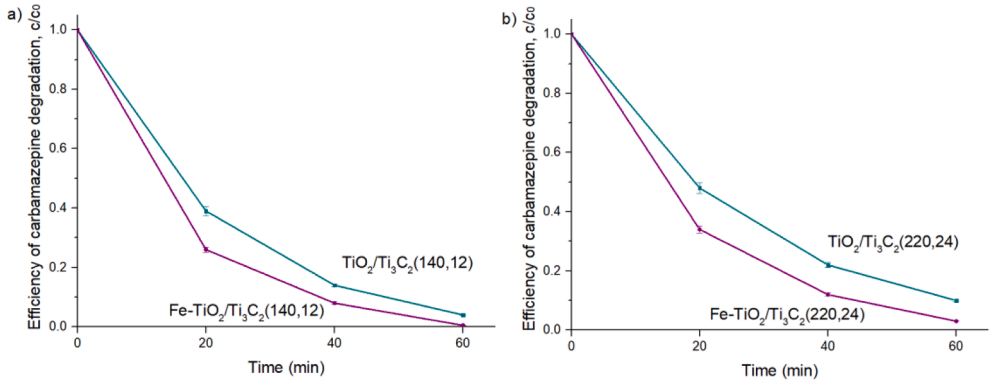

Fig. 15. Carbamazepine degradation for samples a) TiO_2/Ti_3C_2(140,12) and Fe-TiO_2/Ti_3C_2(140,12) b) TiO_2/Ti_3C_2(220,24) and Fe-TiO_2/Ti_3C_2(220,24) within 60 min of irradiation.

were selected for the reusability test. The four subsequent cycles of carbamazepine degradation were performed under UV–Vis irradiation to study the photocatalytic reusability, as presented in Fig. 8S in the Supporting Materials. At the end of each run, the photocatalyst was separated from the reaction suspension by filtration. Afterward, the separated photocatalyst was reused without any treatment. The efficiency of photocatalytic degradation after the 4th cycle decreased by about 15% compared to the 1st cycle. A slight decrease in activity after each irradiation cycle was possibly related to the photocatalyst losses due to the separation process.

Furthermore, the possible changes of photocatalyst's surface due to the deposition of intermediate products were evaluated by analyzing functional groups using the FTIR technique, as shown in Fig. 16. The FTIR spectra of Fe-TiO_2/Ti_3C_2(140,12) composite showed no notable difference between samples before and after the photocatalytic process. For photocatalyst sample before irradiation, only stretching vibrations of Ti-O bonds (620 cm^{-1}) and –OH surface groups (1625 cm^{-1} and 3430 cm^{-1}) were distinguished. In the case of Fe-TiO_2/Ti_3C_2(140,12) sample measured after the photocatalytic process, instead of –OH surface groups, –NH groups were distinguished (broad peak in the region of 3000–3400 cm^{-1}), which probably suggest adsorption of some simple intermediates of carbamazepine degradation on the photocatalyst's surface.

3.3. Mechanism of photocatalytic degradation

To further study the degradation mechanism in the presence of TiO_2-Ti_3C_2 composite, scavengers of the photo-generated electrons, holes and the main reactive oxygen species (·OH, $\cdot O_2^-$) were added into the phenol and carbamazepine solution, respectively. The results are presented in Fig. 17. Introduction of *tert*-butanol as a hydroxyl radicals (·OH) scavenger slightly retarded the photodegradation efficiency. It suggests that ·OH is one of the synergistic active species. Meanwhile, scavenging of superoxide radical anions significantly suppressed both phenol and carbamazepine decomposition rates. Thus, it indicates that $\cdot O_2^-$ plays a crucial role in the photocatalytic degradation mechanism. However, for phenol degradation, the hydroxyl radicals much more contribute to the degradation mechanism, while for carbamazepine superoxide anion radicals.

Furthermore, the addition of $AgNO_3$ as an electron scavenger remarkably increased the effectiveness of organic compounds degradation under UV–Vis light irradiation. Similar phenomena were observed by Samsudin et al. [100] for degradation of methylene blue (MB) with

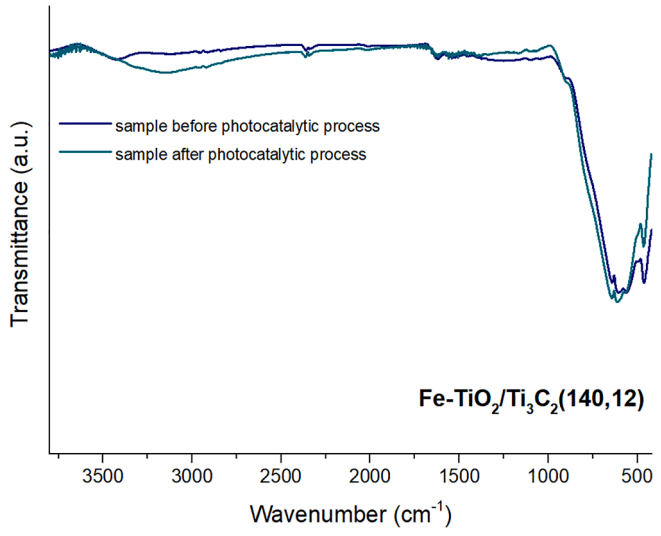

Fig. 16. The FTIR spectra for sample Fe-TiO_2/Ti_3C_2(140,12) measured before and after the photocatalytic process of carbamazepine degradation.

$BiVO_4$ photocatalyst under visible light irradiation. $BiVO_4$ photocatalyst with a higher content of (0 1 0) than (1 1 0) planes was characterized by a higher number of excited electrons located onto (0 1 0) planes. These photoexcited electrons can be easily capped by the electron scavenger leading to inhibition of the electron-hole pairs' recombination. As it was stated by Samsudin et al., when the recombination rate was reduced due to $AgNO_3$, a more significant number of photoexcited electrons may migrate and produce superoxide radicals, which further reacted with MB. Under UV–Vis light irradiation, TiO_2/Ti_3C_2 generates electrons (e^-) and holes (h^+), which participate in the generation of reactive species to decompose contaminants. Scavenging of holes resulted in a decrease in photodegradation, indicating improved electrons separation in the system.

The {0 0 1} facet with a high density of low energy O 2 s states is the only one above the valence band edge of the TiO_2 [101]. Therefore, it is suitable for the oxidation of H_2O to •OH. The phenol degradation mechanism mainly proceeded by ·OH attack at *ortho* substitution, resulting in increased *ortho*-hydroxybenzoquinone formation. It can explain a distinct decrease of k for phenol degradation in the presence of TiO_2 with more exposed {1 0 1} facets combined with Ti_3C_2 - sample TiO_2/Ti_3C_2(140,12). Regarding carbamazepine degradation, it could be assumed that ·OH radicals played a minor role during photocatalytic oxidation reaction. The mainly exposed at TiO_2/Ti_3C_2 surface {1 0 1} facet accumulates electrons and promotes oxygen reduction to $\cdot O_2^-$.

Furthermore, superoxide radicals and hydrogen peroxide led to the formation of other reactive oxygen species: hydroxyl radicals (·OH) and singlet oxygen ($^1O_2$). In turn, it resulted in a constant increase in the degradation efficiency of CBZ. Additionally, Fe-species may readily accept excited electrons, thus reducing electron-hole recombination [102].

Fig. 18 shows a graphical presentation of the photocatalyst band edges position and charge transfer during excitation with a light greater than its bandgap energy. The potential of TiO_2/Ti_3C_2(140,12) and TiO_2/Ti_3C_2(220,24) flat band edge position recorded at −0.69 V and −0.49 V vs. Ag/AgCl/0.1 M KCl, respectively was converted to a value of −0.402 V and −0.20 V vs. NHE. The valence band edge location was estimated according to a value of the flat band edge position and bandgap energy and amounted to 2.598 V vs. NHE for TiO_2/Ti_3C_2(220,24) and 2.198 V vs. NHE for TiO_2/Ti_3C_2(140,12). According to the obtained results, TiO_2/Ti_3C_2(220,24) photocatalyst may more effectively oxidize H_2O to hydroxyl radicals, while TiO_2/Ti_3C_2(140,12) and TiO_2/Ti_3C_2(220,24) can also oxidize H_2O to oxygen and reduce oxygen into superoxide radicals.

The band structure of TiO_2/Ti_3C_2 layered composite correlates with significant inhibition of phenol and carbamazepine degradation in the presence of benzoquinone as a scavenger, suggesting that the degradation mechanism involving superoxide radicals played a crucial role. Furthermore, the presented results correspond with the EPR analysis, where the presence of a high number of Ti^{3+} sites and carbon or oxygen vacancies in the crystal lattice of the TiO_2/Ti_3C_2 was proved. These active sites, where photo-generated electrons react with oxygen, producing highly reactive superoxide anion radicals, may explain this mechanism.

A schematic illustration of the photocatalytic mechanism of carbamazepine degradation on Fe-TiO_2/Ti_3C_2 photocatalyst with co-exposed {0 0 1} and {1 0 1} TiO_2 facets was proposed and presented in Fig. 19. The Ti_3C_2 and Fe-species may readily accept excited electrons [102–103], thus reducing electron-hole recombination. However, in the case of iron oxide particles distributed on {0 0 1} TiO_2 facet, there is limited electron transfer from {1 0 1} facet, due to spatial separation, despite the iron oxide CB band position is located below TiO_2 CB position [104]. Accumulated electrons participate in superoxide anion radicals generation from oxygen as a main reactive oxygen species taking part in the photocatalytic oxidation reaction.

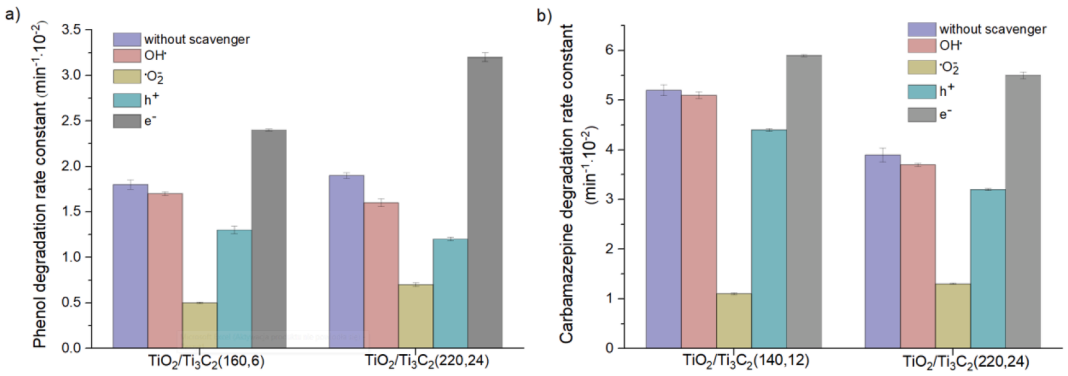

Fig. 17. Degradation rate constant in the presence of scavengers for a) phenol and b) carbamazepine removal.

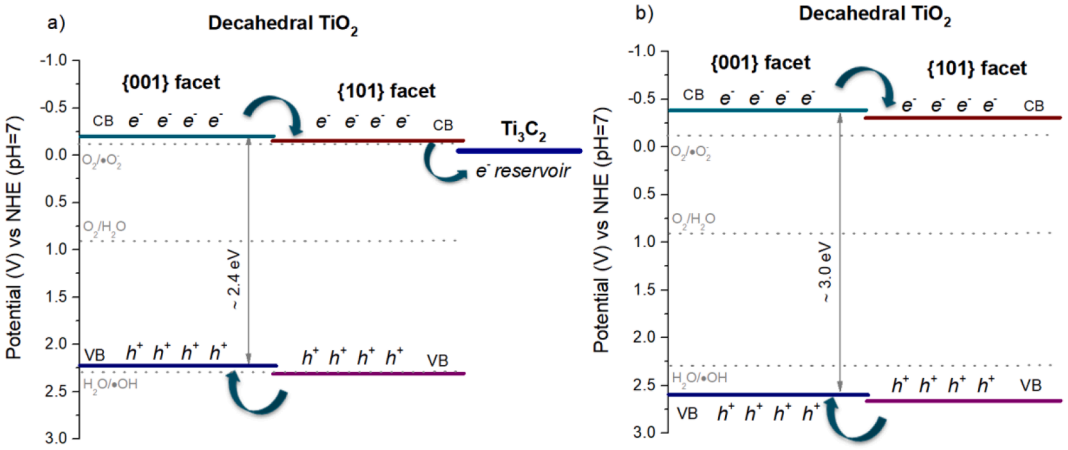

Fig. 18. Schematic representation of a)TiO_2/Ti_3C_2(140,12) and b) TiO_2/Ti_3C_2(220,24) band structure and excitation under UV–Vis light.

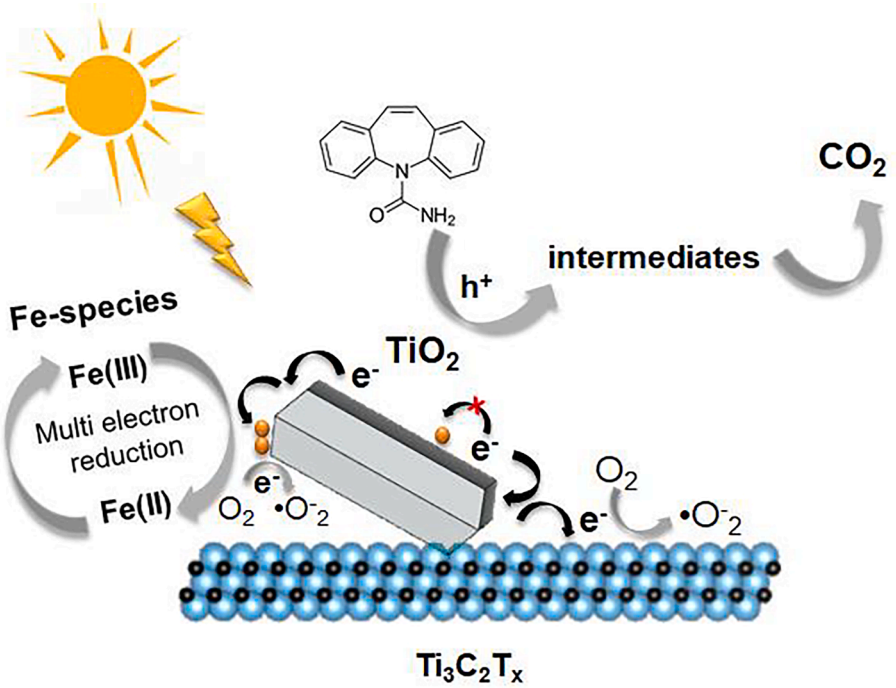

Fig. 19. Schematic illustration of the proposed mechanism of carbamazepine degradation in the presence of Fe-modified TiO_2/Ti_3C_2(140,12) photocatalyst with co-exposed {101} and {001} facets.

4. Conclusions

In summary, TiO_2 nanocomposites were synthesized through the solvothermal method using as a precursor accordion-like MXene compound – $Ti_3C_2T_x$. The controlled oxidation led to the formation of TiO_2 with decahedral morphology and exposed highly active {0 0 1} and {1 0 1} facets on Ti_3C_2 layer. During the study, the influence of time and temperature on the prepared composites' physicochemical and structural properties was determined. The obtained layered composite photocatalysts were characterized by a narrower bandgap ($E_g < 3$ eV), titanium vacancies (Ti^{3+} centers), carbon and oxygen vacancies. The materials synthesized under more severe conditions (the highest reaction temperature of 220°C and prolonged-time) led to the in-situ formation of TiO_2 DAPs derived from the MXene phase, while milder synthesis conditions (temperature below 200°C) led to preserved TiO_2/Ti_3C_2 structure.

The results of photocatalytic activity of phenol and carbamazepine degradation confirmed that composites prepared at lower temperature and with shorter reaction time, i.e., TiO_2/Ti_3C_2(160,6) and TiO_2/Ti_3C_2(140,12) and photocatalysts synthesized at the higher temperature (above 200 °C) and most prolonged time, i.e., TiO_2/Ti_3C_2(200,24), TiO_2/Ti_3C_2(220,12) and TiO_2/Ti_3C_2(220,24) exhibited the most excellent performance. These findings indicate the promoting effect of $Ti_3C_2T_x$ on TiO_2 activity under UV–Vis irradiation, which may act as a reservoir of photo-generated electrons, thus minimizing the recombination rate of electron-hole pairs. Moreover, the morphological properties of decahedral anatase particles with co-exposed {1 0 1} and {0 0 1} facets improve photoelectron transfer, which reduces charge carriers recombination.

The most active samples labeled TiO_2/Ti_3C_2(140,12) and TiO_2/Ti_3C_2(220,24) were further modified with iron. The ternary composite Fe-TiO_2/Ti_3C_2(140,12) showed significantly improved carbamazepine photocatalytic degradation with 100% removal after 60 min of UV–Vis irradiation. The increment in donor density and a positive shift of flat band potential of Fe-modified TiO_2/Ti_3C_2 sample compared to neat TiO_2/Ti_3C_2 contributed to superior photo-oxidation efficiency. Moreover, the photocurrent measurements, emission spectroscopy, and luminescence decay analysis confirmed that samples modified with iron species showed more efficient separation of the photoexcited electron-hole pairs and slower decay indicating long charge carrier lifetimes and metastable donor states.

Declaration of Competing Interest

The authors declare that they have no known competing financial interests or personal relationships that could have appeared to influence the work reported in this paper.

Acknowledgments

This research was financially supported by the Polish National Science Centre (grant no. NCN 2018/30/E/ST5/00845). AZJ acknowledges Polish Ministry of Science and Higher Education grant no. 0525/E-359/STYP/13/2018 Scholarships for outstanding young scientists. We also acknowledge Professor Anna Lisowska-Oleksiak from Gdańsk University of Technology for providing measuring equipment and support in electrochemical analysis.

Appendix A. Supplementary data

Supplementary data to this article can be found online at https://doi.org/10.1016/j.cej.2021.130801.

References

[1] The report "European waters - assessment of status and pressures 2018". European Environment Agency, Publications Office of the European Union, Luxembourg, 2018.
[2] A. Bhandari, R.Y. Surampalli, C.D. Adams, P. Champagne, S.K. Ong, R.D. Tyagi, T. Zhang (Eds.), Contaminants of Emerging Environmental Concern, American Society of Civil Engineers, Reston, VA, 2009.
[3] N. Callaghan, M. O'Callaghan, B. Duggan, M. Feely, Carbamazepine as a single drug in the treatment of epilepsy. A prospective study of serum levels and seizure control. J. Neurol. Neurosurg. Psychiatry 41 (10) (1978) 907–912, https://doi.org/10.1136/jnnp.41.10.907.
[4] C. Gadipelly, A. Pérez-González, G.D. Yadav, I. Ortiz, R. Ibáñez, V.K. Rathod, K. V. Marathe, Pharmaceutical Industry Wastewater: Review of the Technologies for Water Treatment and Reuse, Ind. Eng. Chem. Res. 53 (29) (2014) 11571–11592, https://doi.org/10.1021/ie501210j.
[5] Y. Zhang, S.-U. Geißen, C. Gal, Carbamazepine and diclofenac: Removal in wastewater treatment plants and occurrence in water bodies, Chemosphere 73 (8) (2008) 1151–1161, https://doi.org/10.1016/j.chemosphere.2008.07.086.
[6] Benoît Ferrari, N. Paxéus, R.L. Giudice, A. Pollio, J. Garric, Ecotoxicological impact of pharmaceuticals found in treated wastewaters: study of carbamazepine, clofibric acid, and diclofenac, Ecotoxicol. Environ. Saf. 55 (3) (2003) 359–370, https://doi.org/10.1016/S0147-6513(02)00082-9.
[7] S. Wang, J. Wang, Carbamazepine degradation by gamma irradiation coupled to biological treatment, J. Hazard. Mater. 321 (2017) 639–646, https://doi.org/10.1016/j.jhazmat.2016.09.053.
[8] M. Yao, L. Duan, J. Wei, F. Qian, S.W. Hermanowicz, Carbamazepine removal from wastewater and the degradation mechanism in a submerged forward osmotic membrane bioreactor, Bioresour. Technol. 314 (2020) 123732, https://doi.org/10.1016/j.biortech.2020.123732.
[9] M. Chtourou, M. Mallek, M. Dalmau, J. Mamo, E. Santos-Clotas, A.B. Salah, K. Walha, V. Salvadó, H. Monclús, Triclosan, carbamazepine and caffeine removal by activated sludge system focusing on membrane bioreactor, Process Saf. Environ. Prot. 118 (2018) 1–9, https://doi.org/10.1016/j.psep.2018.06.019.
[10] A.G. Pekel, E. Kurtulbaş, İ. Toprakçı, S. Şahin, Menthol-based deep eutectic solvent for the separation of carbamazepine: reactive liquid-liquid extraction, Biomass Convers. Biorefinery (2020), https://doi.org/10.1007/s13399-020-00707-z.
[11] S.K. Alharbi, W.E. Price, J. Kang, T. Fujioka, L.D. Nghiem, Ozonation of carbamazepine, diclofenac, sulfamethoxazole and trimethoprim and formation of major oxidation products, Desalin. Water Treat. 57 (60) (2016) 29340–29351, https://doi.org/10.1080/19443994.2016.1172986.
[12] L. Yang, L. Liang, L. Wang, J. Zhu, S. Gao, X. Xia, Accelerated photocatalytic oxidation of carbamazepine by a novel 3D hierarchical protonated g-C_3N_4/BiOBr heterojunction: Performance and mechanism, Appl. Surf. Sci. 473 (2019) 527–539, https://doi.org/10.1016/j.apsusc.2018.12.180.
[13] Z. Wang, C. Li, K. Domen, Recent developments in heterogeneous photocatalysts for solar-driven overall water splitting, Chem. Soc. Rev. 48 (7) (2019) 2109–2125, https://doi.org/10.1039/C8CS00542G.
[14] W. Wang, C. Zhou, Y. Yang, G. Zeng, C. Zhang, Y. Zhou, J. Yang, D. Huang, H. Wang, W. Xiong, X. Li, Y. Fu, Z. Wang, Q. He, M. Jia, H. Luo, Carbon nitride based photocatalysts for solar photocatalytic disinfection, can we go further? Chem. Eng. J. 404 (2021) 126540, https://doi.org/10.1016/j.cej.2020.126540.
[15] W. Zhang, A.R. Mohamed, W.-J. Ong, Z-Scheme Photocatalytic Systems for Carbon Dioxide Reduction: Where Are We Now? Angew. Chem. Int. Ed. 59 (51) (2020) 22894–22915, https://doi.org/10.1002/anie.201914925.
[16] S. Zhang, B. Li, X. Wang, G. Zhao, B. Hu, Z. Lu, T. Wen, J. Chen, X. Wang, Recent developments of two-dimensional graphene-based composites in visible-light photocatalysis for eliminating persistent organic pollutants from wastewater, Chem. Eng. J. 390 (2020) 124642, https://doi.org/10.1016/j.cej.2020.124642.
[17] R. Qian, H. Zong, J. Schneider, G. Zhou, T. Zhao, Y. Li, J. Yang, D.W. Bahnemann, J.H. Pan, Charge carrier trapping, recombination and transfer during TiO_2 photocatalysis: An overview, Catal. Today 335 (2019) 78–90, https://doi.org/10.1016/j.cattod.2018.10.053.
[18] Wysocka, I., Kowalska, E., Ryl, J., Nowaczyk, G., Zielińska-Jurek, A. Morphology, Photocatalytic and Antimicrobial Properties of TiO2 Modified with Mono- and Bimetallic Copper, Platinum and Silver Nanoparticles. Nanomaterials 9 (2019) 1129. https://doi.org/10.3390/nano9081129.
[19] Y. Li, Y.-L. Li, B. Sa, R. Ahuja, Review of two-dimensional materials for photocatalytic water splitting from a theoretical perspective, Catal. Sci. Technol. 7 (3) (2017) 545–559, https://doi.org/10.1039/C6CY02178F.
[20] B. Luo, G. Liu, L. Wang, Recent advances in 2D materials for photocatalysis, Nanoscale 8 (13) (2016) 6904–6920, https://doi.org/10.1039/C6NR00546B.
[21] X. Chia, M. Pumera, Characteristics and performance of two-dimensional materials for electrocatalysis, Nat. Catal. 1 (12) (2018) 909–921, https://doi.org/10.1038/s41929-018-0181-7.
[22] Buckley, D. J., Black, N.C.G., Castanon, E.G., Melios, C., Hardman, M., Kazakova O. Frontiers of graphene and 2D material-based gas sensors for environmental monitoring. 2D Mater. 7 (2020) 032002. https://doi.org/10.1088/2053-1583/ab7bc5.
[23] Y. Zhu, L. Peng, Z. Fang, C. Yan, X. Zhang, G. Yu, Structural Engineering of 2D Nanomaterials for Energy Storage and Catalysis, Adv. Mater. 30 (15) (2018) 1706347, https://doi.org/10.1002/adma.201706347.
[24] C. Du, B.o. Yan, Z. Lin, G. Yang, Enhanced carrier separation and increased electron density in 2D heavily N-doped ZnIn 2 S 4 for photocatalytic hydrogen

production, J. Mater. Chem. A 8 (1) (2020) 207–217, https://doi.org/10.1039/C9TA11318E.
[25] Y. Zhao, S. Zhang, R. Shi, G.I.N. Waterhouse, J. Tang, T. Zhang, Two-dimensional photocatalyst design: A critical review of recent experimental and computational advances, Mater. Today 34 (2020) 78–91, https://doi.org/10.1016/j.mattod.2019.10.022.
[26] S.V.P. Vattikuti, J. Shim, C. Byon, 1D Bi_2S_3 nanorod/2D e-WS_2 nanosheet heterojunction photocatalyst for enhanced photocatalytic activity, J. Solid State Chem. 258 (2018) 526–535, https://doi.org/10.1016/j.jssc.2017.11.017.
[27] Y. Yang, X. Li, C. Lu, W. Huang, G-C3N4 Nanosheets Coupled with TiO2 Nanosheets as 2D/2D Heterojunction Photocatalysts Toward High Photocatalytic Activity for Hydrogen Production, Catal. Lett. 149 (10) (2019) 2930–2939, https://doi.org/10.1007/s10562-019-02805-8.
[28] Y. Li, P. Zhang, D. Wan, C. Xue, J. Zhao, G. Shao, Direct evidence of 2D/1D heterojunction enhancement on photocatalytic activity through assembling MoS_2 nanosheets onto super-long TiO_2 nanofibers, Appl. Surf. Sci. 504 (2020) 144361, https://doi.org/10.1016/j.apsusc.2019.144361.
[29] H. Fan, H. Zhou, W. Li, S. Gu, G. Zhou, Facile fabrication of 2D/2D step-scheme In_2S_3/$Bi_2O_2CO_3$ heterojunction towards enhanced photocatalytic activity, Appl. Surf. Sci. 504 (2020) 144351, https://doi.org/10.1016/j.apsusc.2019.144351.
[30] K. Hantanasirisakul, Y. Gogotsi, Electronic and Optical Properties of 2D Transition Metal Carbides and Nitrides (MXenes), Adv. Mater. 30 (52) (2018) 1804779, https://doi.org/10.1002/adma.201804779.
[31] C. Wei, H. Fei, Y. Tian, Y. An, H. Guo, J. Feng, Y. Qian, Isotropic Li nucleation and growth achieved by an amorphous liquid metal nucleation seed on MXene framework for dendrite-free Li metal anode, Energy Storage Mater. 26 (2020) 223–233, https://doi.org/10.1016/j.ensm.2020.01.005.
[32] Y. Tian, Y. An, C. Wei, Y. Tao, Y. Zhang, H. Jiang, L. Tan, J. Feng, Y. Qian, Stable and dendrite-free lithium metal anodes enabled by carbon paper incorporated with ultrafine lithiophilic TiO2 derived from MXene and carbon dioxide, Chem. Eng. J. 406 (2021) 126836, https://doi.org/10.1016/j.cej.2020.126836.
[33] H.A. Tahini, X. Tan, S.C. Smith, The origin of low workfunctions in OH terminated MXenes, Nanoscale 9 (21) (2017) 7016–7020, https://doi.org/10.1039/C7NR01601H.
[34] R. Xiao, C. Zhao, Z. Zou, Z. Chen, L. Tian, H. Xu, H. Tang, Q. Liu, Z. Lin, X. Yang, In situ fabrication of 1D CdS nanorod/2D Ti_3C_2 MXene nanosheet Schottky heterojunction toward enhanced photocatalytic hydrogen evolution, Appl. Catal. B 268 (2020) 118382, https://doi.org/10.1016/j.apcatb.2019.118382.
[35] S. Cao, B. Shen, T. Tong, J. Fu, J. Yu, 2D/2D Heterojunction of Ultrathin MXene/Bi 2 WO 6 Nanosheets for Improved Photocatalytic CO 2 Reduction, Adv. Funct. Mater. 28 (21) (2018) 1800136, https://doi.org/10.1002/adfm.201800136.
[36] X. Xie, N. Zhang, Z.-R. Tang, M. Anpo, Y.-J. Xu, Ti3C2Tx MXene as a Janus cocatalyst for concurrent promoted photoactivity and inhibited photocorrosion, Appl. Catal. B 237 (2018) 43–49, https://doi.org/10.1016/j.apcatb.2018.05.070.
[37] L. Tie, S. Yang, C. Yu, H. Chen, Y. Liu, S. Dong, J. Sun, J. Sun, In situ decoration of ZnS nanoparticles with Ti_3C_2 MXene nanosheets for efficient photocatalytic hydrogen evolution, J. Colloid Interface Sci. 545 (2019) 63–70, https://doi.org/10.1016/j.jcis.2019.03.014.
[38] T. Cai, L. Wang, Y. Liu, S. Zhang, W. Dong, H. Chen, X. Yi, J. Yuan, X. Xia, C. Liu, S. Luo, Ag_3PO_4/Ti_3C_2 MXene interface materials as a Schottky catalyst with enhanced photocatalytic activities and anti-photocorrosion performance, Appl. Catal. B 239 (2018) 545–554, https://doi.org/10.1016/j.apcatb.2018.08.053.
[39] Y. Sun, D.i. Jin, Y. Sun, X. Meng, Y.u. Gao, Y. Dall'Agnese, G. Chen, X.-F. Wang, g-C 3 N 4 /Ti 3 C 2 T x (MXenes) composite with oxidized surface groups for efficient photocatalytic hydrogen evolution, J. Mater. Chem. A 6 (19) (2018) 9124–9131, https://doi.org/10.1039/C8TA02706D.
[40] Z. Zeng, Y. Yan, J. Chen, P. Zan, Q. Tian, P. Chen, Boosting the Photocatalytic Ability of Cu 2 O Nanowires for CO 2 Conversion by MXene Quantum Dots, Adv. Funct. Mater. 29 (2) (2019) 1806500, https://doi.org/10.1002/adfm.201806500.
[41] C. Liu, Q. Xu, Q. Zhang, Y. Zhu, M. Ji, Z. Tong, W. Hou, Y.u. Zhang, J. Xu, Layered BiOBr/Ti_3C_2 MXene composite with improved visible-light photocatalytic activity, J. Mater. Sci. 54 (3) (2019) 2458–2471, https://doi.org/10.1007/s10853-018-2990-0.
[42] H. Zhang, M. Li, J. Cao, Q. Tang, P. Kang, C. Zhu, M. Ma, 2D a-Fe_2O_3 doped Ti_3C_2 MXene composite with enhanced visible light photocatalytic activity for degradation of Rhodamine B, Ceram. Int. 44 (16) (2018) 19958–19962, https://doi.org/10.1016/j.ceramint.2018.07.262.
[43] J. Low, L. Zhang, T. Tong, B. Shen, J. Yu, TiO_2/MXene Ti_3C_2 composite with excellent photocatalytic CO_2 reduction activity, J. Catal. 361 (2018) 255–266, https://doi.org/10.1016/j.jcat.2018.03.009.
[44] J. Yin, F. Zhan, T. Jiao, W. Wang, G. Zhang, J. Jiao, G. Jiang, Q. Zhang, J. Gu, Q. Peng, Facile preparation of self-assembled MXene@Au@CdS nanocomposite with enhanced photocatalytic hydrogen production activity自组装纳米复合材料MXene@Au@CdS的制备及其光催化制氢活性, Sci. China Mater. 63 (11) (2020) 2228–2238, https://doi.org/10.1007/s40843-020-1299-4.
[45] K. Li, T. Jiao, R. Xing, G. Zou, J. Zhou, L. Zhang, Q. Peng, Fabrication of tunable hierarchical MXene@AuNPs nanocomposites constructed by self-reduction reactions with enhanced catalytic performances自还原反应制备可调层状MXene@AuNPs复合材料以提高催化性能, Sci. China Mater. 61 (5) (2018) 728–736, https://doi.org/10.1007/s40843-017-9196-8.
[46] X. Huang, R. Wang, T. Jiao, G. Zou, F. Zhan, J. Yin, L. Zhang, J. Zhou, Q. Peng, Facile Preparation of Hierarchical AgNP-Loaded MXene/Fe 3 O 4 /Polymer Nanocomposites by Electrospinning with Enhanced Catalytic Performance for Wastewater Treatment, ACS Omega 4 (1) (2019) 1897–1906, https://doi.org/10.1021/acsomega.8b03615.
[47] J. Yin, B. Ge, T. Jiao, Z. Qin, M. Yu, L. Zhang, Q. Zhang, Q. Peng, Self-Assembled Sandwich-like MXene-Derived Composites as Highly Efficient and Sustainable Catalysts for Wastewater Treatment, Langmuir 37 (3) (2021) 1267–1278, https://doi.org/10.1021/acs.langmuir.0c03297.s001.
[48] K. Li, T. Jiao, R. Xing, G. Zou, Q. Zhao, J. Zhou, L. Zhang, Q. Peng, Fabrication of hierarchical MXene-based AuNPs-containing core–shell nanocomposites for high efficient catalysts, Green Energy Environ. 3 (2) (2018) 147–155, https://doi.org/10.1016/j.gee.2017.11.004.
[49] M.A. Iqbal, S.I. Ali, F. Amin, A. Tariq, M.Z. Iqbal, S. Rizwan, La- and Mn-Codoped Bismuth Ferrite/Ti 3 C 2 MXene Composites for Efficient Photocatalytic Degradation of Congo Red Dye, ACS Omega 4 (5) (2019) 8661–8668, https://doi.org/10.1021/acsomega.9b00493.
[50] C.e. Cui, R. Guo, H. Xiao, E. Ren, Q. Song, C. Xiang, X. Lai, J. Lan, S. Jiang, Bi_2WO_6/Nb_2CT_x MXene hybrid nanosheets with enhanced visible-light-driven photocatalytic activity for organic pollutants degradation, Appl. Surf. Sci. 505 (2020) 144595, https://doi.org/10.1016/j.apsusc.2019.144595.
[51] Y. Li, Z. Yin, G. Ji, Z. Liang, Y. Xue, Y. Guo, J. Tian, X. Wang, H. Cui, 2D/2D/2D heterojunction of Ti_3C_2 MXene/MoS_2 nanosheets/TiO_2 nanosheets with exposed (001) facets toward enhanced photocatalytic hydrogen production activity, Appl. Catal. B 246 (2019) 12–20, https://doi.org/10.1016/j.apcatb.2019.01.051.
[52] X. An, W. Wang, J. Wang, H. Duan, J. Shi, X. Yu, The synergetic effects of Ti 3 C 2 MXene and Pt as co-catalysts for highly efficient photocatalytic hydrogen evolution over g-C 3 N 4, PCCP 20 (16) (2018) 11405–11411, https://doi.org/10.1039/C8CP01123K.
[53] J. Ran, G. Gao, F.-T. Li, T.-Y. Ma, A. Du, S.-Z. Qiao, Ti_3C_2 MXene co-catalyst on metal sulfide photo-absorbers for enhanced visible-light photocatalytic hydrogen production, Nat. Commun. 8 (1) (2017), https://doi.org/10.1038/ncomms13907.
[54] M. Kowalkińska, S. Dudziak, J. Karczewski, J. Ryl, G. Trykowski, A. Zielińska-Jurek, Facet effect of TiO_2 nanostructures from $TiOF_2$ and their photocatalytic activity, Chem. Eng. J. 404 (2021) 126493, https://doi.org/10.1016/j.cej.2020.126493.
[55] J. Wang, B. Liu, K. Nakata, Effects of crystallinity, {001}/{101} ratio, and Au decoration on the photocatalytic activity of anatase TiO_2 crystals, Chin. J. Catal. 40 (3) (2019) 403–412, https://doi.org/10.1016/S1872-2067(18)63174-2.
[56] J. Yu, J. Low, W. Xiao, P. Zhou, M. Jaroniec, Enhanced Photocatalytic CO 2 -Reduction Activity of Anatase TiO 2 by Coexposed {001} and {101} Facets, J. Am. Chem. Soc. 136 (25) (2014) 8839–8842, https://doi.org/10.1021/ja5044787.
[57] Y. Cao, Q. Deng, Z. Liu, D. Shen, T. Wang, Q. Huang, S. Du, N. Jiang, C.-T. Lin, J. Yu, Enhanced thermal properties of poly(vinylidene fluoride) composites with ultrathin nanosheets of MXene, RSC Adv. 7 (33) (2017) 20494–20501, https://doi.org/10.1039/C7RA00184C.
[58] M. Naguib, M. Kurtoglu, V. Presser, J. Lu, J. Niu, M. Heon, L. Hultman, Y. Gogotsi, M.W. Barsoum, Two-Dimensional Nanocrystals Produced by Exfoliation of Ti_3AlC_2, Adv. Mater. 23 (37) (2011) 4248–4253, https://doi.org/10.1002/adma.201102306.
[59] Z. Wei, M. Janczarek, M. Endo, K. Wang, A. Balčytis, A. Nitta, M.G. Méndez-Medrano, C. Colbeau-Justin, S. Juodkazis, B. Ohtani, E. Kowalska, Noble metal-modified faceted anatase titania photocatalysts: Octahedron versus decahedron, Appl. Catal. B 237 (2018) 574–587, https://doi.org/10.1016/j.apcatb.2018.06.027.
[60] M. Shen, L. Zhang, M. Wang, J. Tian, X. Jin, L. Guo, L. Wang, J. Shi, Carbon-vacancy modified graphitic carbon nitride: enhanced CO 2 photocatalytic reduction performance and mechanism probing, J. Mater. Chem. A 7 (4) (2019) 1556–1563, https://doi.org/10.1039/C8TA09302D.
[61] C. Peng, H. Wang, H. Yu, F. Peng, (111) TiO 2-x /Ti 3 C 2 : Synergy of active facets, interfacial charge transfer and Ti 3+ doping for enhance photocatalytic activity, Mater. Res. Bull. 89 (2017) 16–25, https://doi.org/10.1016/j.materresbull.2016.12.049.
[62] P.K. Kalambate, Dhanjai, A. Sinha, Y. Li, Y. Shen, Y. Huang, An electrochemical sensor for ifosfamide, acetaminophen, domperidone, and sumatriptan based on self-assembled MXene/MWCNT/chitosan nanocomposite thin film, Microchim. Acta 187 (7) (2020), https://doi.org/10.1007/s00604-020-04366-9.
[63] F. Kong, X. He, Q. Liu, X. Qi, Y. Zheng, R. Wang, Y. Bai, Improving the electrochemical properties of MXene Ti_3C_2 multilayer for Li-ion batteries by vacuum calcination, Electrochim. Acta 265 (2018) 140–150, https://doi.org/10.1016/j.electacta.2018.01.196.
[64] X. Zhang, J.F. Zhang, S.X. Yang, H.Y. Cao, H.J. Huang, W. Jiang, Electrocatalytic Performance of Palladium Nanoparticle Supported by Two-dimensional Titanium Carbide-CNT Composites, J. Inorg. Mater. 33 (2018) 206–212.
[65] Y.-Q. Cao, T.-Q. Zi, X.-R. Zhao, C. Liu, Q. Ren, J.-B. Fang, W.-M. Li, A.-D. Li, Enhanced visible light photocatalytic activity of Fe_2O_3 modified TiO_2 prepared by atomic layer deposition, Sci. Rep. 10 (1) (2020), https://doi.org/10.1038/s41598-020-70352-z.
[66] U. Balachandran, N.G. Eror, Raman spectra of titanium dioxide, J. Solid State Chem. 42 (3) (1982) 276–282, https://doi.org/10.1016/0022-4596(82)90006-8.
[67] C.Y. Xu, P.X. Zhang, L. Yan, Blue shift of Raman peak from coated TiO_2 nanoparticles, J. Raman Spectrosc. 32 (10) (2001) 862–865, https://doi.org/10.1002/jrs.773.
[68] W. Vallejo, A. Rueda, C. Díaz-Uribe, C. Grande, P. Quintana, Photocatalytic activity of graphene oxide–TiO 2 thin films sensitized by natural dyes extracted from Bactris guineensis, R. Soc. Open Sci. 6 (3) (2019) 181824, https://doi.org/10.1098/rsos.181824.
[69] S. Mohajernia, P. Andryskova, G. Zoppellaro, S. Hejazi, S. Kment, R. Zboril, J. Schmidt, P. Schmuki, Influence of Ti 3+ defect-type on heterogeneous

photocatalytic H 2 evolution activity of TiO 2, J. Mater. Chem. A 8 (3) (2020) 1432–1442, https://doi.org/10.1039/C9TA10855F.
[70] Y.i. Zhang, J. Di, P. Ding, J. Zhao, K. Gu, X. Chen, C. Yan, S. Yin, J. Xia, H. Li, Ultrathin g-C_3N_4 with enriched surface carbon vacancies enables highly efficient photocatalytic nitrogen fixation, J. Colloid Interface Sci. 553 (2019) 530–539, https://doi.org/10.1016/j.jcis.2019.06.012.
[71] X. Liang, G. Wang, X. Dong, G. Wang, H. Ma, X. Zhang, Graphitic Carbon Nitride with Carbon Vacancies for Photocatalytic Degradation of Bisphenol A, ACS Appl. Nano Mater. 2 (1) (2019) 517–524, https://doi.org/10.1021/acsanm.8b02089.
[72] Y. Li, W. Ho, K. Lv, B. Zhu, S.C. Lee, Carbon vacancy-induced enhancement of the visible light-driven photocatalytic oxidation of NO over g-C 3 N 4 nanosheets, Appl. Surf. Sci. 430 (2018) 380–389, https://doi.org/10.1016/j.apsusc.2017.06.054.
[73] H. Hirakawa, M. Hashimoto, Y. Shiraishi, T. Hirai, Photocatalytic Conversion of Nitrogen to Ammonia with Water on Surface Oxygen Vacancies of Titanium Dioxide, J. Am. Chem. Soc. 139 (31) (2017) 10929–10936, https://doi.org/10.1021/jacs.7b06634.s001.
[74] Y. Xu, S. Wu, P. Wan, J. Sun, Z.D. Hood, Introducing Ti 3+ defects based on lattice distortion for enhanced visible light photoreactivity in TiO 2 microspheres, RSC Adv. 7 (52) (2017) 32461–32467, https://doi.org/10.1039/C7RA04885H.
[75] F.J. Knorr, C.C. Mercado, J.L. McHale, Trap-State Distributions and Carrier Transport in Pure and Mixed-Phase TiO 2 : Influence of Contacting Solvent and Interphasial Electron Transfer, J. Phys. Chem. C 112 (33) (2008) 12786–12794, https://doi.org/10.1021/jp8039934.
[76] X. Wang, S. Shen, Z. Feng, C. Li, Time-resolved photoluminescence of anatase/rutile TiO2 phase junction revealing charge separation dynamics, Chin. J. Catal. 37 (12) (2016) 2059–2068, https://doi.org/10.1016/S1872-2067(16)62574-3.
[77] K. Fujihara, S. Izumi, T. Ohno, M. Matsumura, Time-resolved photoluminescence of particulate TiO2 photocatalysts suspended in aqueous solutions, J. Photochem. Photobiol., A 132 (1-2) (2000) 99–104, https://doi.org/10.1016/S1010-6030(00)00204-5.
[78] A. Saha, A. Moya, A. Kahnt, D. Iglesias, S. Marchesan, R. Wannemacher, M. Prato, J.J. Vilatela, D.M. Guldi, Interfacial charge transfer in functionalized multi-walled carbon nanotube@TiO 2 nanofibres, Nanoscale 9 (23) (2017) 7911–7921, https://doi.org/10.1039/C7NR00759K.
[79] R. Brüninghoff, K. Wenderich, J.P. Korterik, B.T. Mei, G. Mul, A. Huijser, Time-Dependent Photoluminescence of Nanostructured Anatase TiO 2 and the Role of Bulk and Surface Processes, J. Phys. Chem. C 123 (43) (2019) 26653–26661, https://doi.org/10.1021/acs.jpcc.9b06890.s001.
[80] H. Cui, W. Zhao, C. Yang, H. Yin, T. Lin, Y. Shan, Y. Xie, H. Gu, F. Huang, Black TiO 2 nanotube arrays for high-efficiency photoelectrochemical water-splitting, J. Mater. Chem. A 2 (23) (2014) 8612–8616, https://doi.org/10.1039/C4TA00176A.
[81] P. Xu, T.J. Milstein, T.E. Mallouk, Flat-Band Potentials of Molecularly Thin Metal Oxide Nanosheets, ACS Appl. Mater. Interfaces 8 (18) (2016) 11539–11547, https://doi.org/10.1021/acsami.6b02901.s001.
[82] B.M. Bresolin, N.O. Balayeva, L.I. Granone, R. Dillert, D.W. Bahnemann, M. Sillanpää, Anchoring lead-free halide $Cs_3Bi_2I_9$ perovskite on UV100–TiO_2 for enhanced photocatalytic performance, Sol. Energy Mater. Sol. Cells 204 (2020) 1–11, https://doi.org/10.1016/j.solmat.2019.110214.
[83] Bisquert, J. Nanostructured energy devices: equilibrium concepts and kinetics. CRC Press, Boca Raton, 2014. https://doi.org/10.1201/b17613.
[84] Y. Li, D. Zhang, X. Feng, Y. Liao, Q. Wen, Q. Xiang, Truncated octahedral bipyramidal TiO2/MXen Ti3C2 hybrids with enhanced photocatalytic H2 production activity, Nanoscale Adv. 1 (2019) 1812–1818, https://doi.org/10.1039/C9NA00023B.
[85] Q. Liu, X. Tan, S. Wang, F. Ma, H. Znad, Z. Shen, L. Liu, S. Liu, MXene as a non-metal charge mediator in 2D layered CdS@Ti 3 C 2 @TiO 2 composites with superior Z-scheme visible light-driven photocatalytic activity, Environ. Sci. Nano 6 (10) (2019) 3158–3169, https://doi.org/10.1039/C9EN00567F.
[86] X. Bao, H. Li, Z. Wang, F. Tong, M.u. Liu, Z. Zheng, P. Wang, H. Cheng, Y. Liu, Y. Dai, Y. Fan, Z. Li, B. Huang, TiO2/Ti3C2 as an efficient photocatalyst for selective oxidation of benzyl alcohol to benzaldehyde, Appl. Catal. B 286 (2021) 119885, https://doi.org/10.1016/j.apcatb.2021.119885.
[87] Y. Liu, H. Zeng, Y. Chai, R. Yuan, H. Liu, Ti 3 C 2 /BiVO 4 Schottky junction as a signal indicator for ultrasensitive photoelectrochemical detection of VEGF 165, Chem. Commun. 55 (91) (2019) 13729–13732, https://doi.org/10.1039/C9CC07108C.
[88] Y. Zhuang, Y. Liu, X. Meng, Fabrication of TiO2 nanofibers/MXene Ti3C2 nanocomposites for photocatalytic H2 evolution by electrostatic self-assembly, Appl. Surf. Sci. 496 (2019) 143647, https://doi.org/10.1016/j.apsusc.2019.143647.
[89] M. Kaneko, Anatase TiO_2 adsorption on 3-aminopropyltrimethoxysilane-modified Al or glass surfaces, Heliyon 5 (2019), e01734, https://doi.org/10.1016/j.heliyon.2019.e0173.
[90] Y. Fu, F. Ding, J. Chen, M. Liu, X. Zhang, C. Du, S. Si, Label-free and near-zero-background-noise photoelectrochemical assay of methyltransferase activity based on a Bi 2 S 3 /Ti 3 C 2 Schottky junction, Chem. Commun. 56 (43) (2020) 5799–5802, https://doi.org/10.1039/D0CC01835J.
[91] M. Shah, Y. Zhu, X. Fan, J. Zhao, Y. Li, S. Asim, C. Wang, Facile Synthesis of Defective TiO 2–x Nanocrystals with High Surface Area and Tailoring Bandgap for Visible-light Photocatalysis, Sci. Rep. 5 (2015) 1–8, https://doi.org/10.1038/srep15804.
[92] C. Randorn, J.T.S. Irvine, Synthesis and visible light photoactivity of a high temperature stable yellow TiO2 photocatalyst, J. Mater. Chem. 20 (39) (2010) 8700, https://doi.org/10.1039/c0jm01370f.
[93] L.i. Ding, Y. Wei, Y. Wang, H. Chen, J. Caro, H. Wang, A Two-Dimensional Lamellar Membrane: MXene Nanosheet Stacks, Angew. Chem. Int. Ed. 56 (7) (2017) 1825–1829, https://doi.org/10.1002/anie.201609306.
[94] M. Kosmulski, P. Próchniak, J.B. Rosenholm, Letter: The IEP of Carbonate-Free Neodymium(III) Oxide, J. Dispersion Sci. Technol. 30 (5) (2009) 589–591, https://doi.org/10.1080/01932690902766319.
[95] G. Serdaroğlu, J.V. Ortiz, Ab Initio Calculations on some Antiepileptic Drugs such as Phenytoin, Phenbarbital, Ethosuximide and Carbamazepine, Struct. Chem. 28 (4) (2017) 957–964, https://doi.org/10.1007/s11224-016-0898-3.
[96] X. Xiao, S. Tu, M. Lu, H. Zhong, C. Zheng, X. Zuo, J. Nan, Discussion on the reaction mechanism of the photocatalytic degradation of organic contaminants from a viewpoint of semiconductor photo-induced electrocatalysis, Appl. Catal. B 198 (2016) 124–132, https://doi.org/10.1016/j.apcatb.2016.05.042.
[97] A. Shahzad, K. Rasool, M. Nawaz, W. Miran, J. Jang, M. Moztahida, K. A. Mahmoud, D.S. Lee, Heterostructural TiO_2/$Ti_3C_2T_x$ (MXene) for photocatalytic degradation of antiepileptic drug carbamazepine, Chem. Eng. J. 349 (2018) 748–755, https://doi.org/10.1016/j.cej.2018.05.148.
[98] H. Tada, Q. Jin, H. Nishijima, H. Yamamoto, M. Fujishima, S.-I. Okuoka, T. Hattori, Y. Sumida, H. Kobayashi, Titanium(IV) Dioxide Surface-Modified with Iron Oxide as a Visible Light Photocatalyst, Angew. Chem. Int. Ed. 50 (15) (2011) 3501–3505, https://doi.org/10.1002/anie.201007869.
[99] E. Donner, T. Kosjek, S. Qualmann, K.O. Kusk, E. Heath, D.M. Revitt, A. Ledin, H. R. Andersen, Ecotoxicity of carbamazepine and its UV photolysis transformation products, Sci. Total Environ. 443 (2013) 870–876, https://doi.org/10.1016/j.scitotenv.2012.11.059.
[100] M. Fakhrul Ridhwan Samsudin, L. Tau Siang, S. Sufian, R. Bashiri, N. Muti Mohamed, R. Mahirah Ramli, Exploring the role of electron-hole scavengers on optimizing the photocatalytic performance of $BiVO_4$, Mater. Today:. Proc. 5 (10) (2018) 21703–21709, https://doi.org/10.1016/j.matpr.2018.07.022.
[101] K. Zhao, Q.Q. Liu, X.C. Wang, Z. Deng, Y.X. Lv, J.L. Zhu, F.Y. Li, C.Q. Jin, Superconductivity above 33 K in (Ca 1 − x Na x)Fe 2 As 2, J. Phys.: Condens. Matter 22 (22) (2010) 222203, https://doi.org/10.1088/0953-8984/22/22/222203.
[102] H. Baniamerian, M. Safavi, M. Alvarado-Morales, P. Tsapekos, I. Angelidaki, S. Shokrollahzadeh, Photocatalytic inactivation of Vibrio fischeri using Fe2O3-TiO2-based nanoparticles, Environ. Res. 166 (2018) 497–506, https://doi.org/10.1016/j.envres.2018.06.011.
[103] G. Huang, S. Li, L. Liu, L. Zhu, Q. Wang, Ti3C2 MXene-modified Bi2WO6 nanoplates for efficient photodegradation of volatile organic compounds, Appl. Surf. Sci. 503 (2020) 144183, https://doi.org/10.1016/j.apsusc.2019.144183.
[104] C. Liu, R. Tong, Z. Xu, Q. Kuang, Z. Xie, L. Zheng, RSC Adv. 6 (2016) 29794, https://doi.org/10.1039/C6RA04552A.